BIOPHYSICS

Conformational plasticity of mitochondrial VDAC2 controls the kinetics of its interaction with cytosolic proteins

William M. Rosencrans[1,2,3], Harisankar Khuntia[4], Motahareh Ghahari Larimi[1,5], Radhakrishnan Mahalakshmi[6], Tsyr-Yan Yu[4], Sergey M. Bezrukov[1], Tatiana K. Rostovtseva[1]*

The voltage-dependent anion channel (VDAC) is a key conduit of the mitochondrial outer membrane for water-soluble metabolites and ions. Among the three mammalian isoforms, VDAC2 is unique because of its embryonic lethality upon knockout. Using single-molecule electrophysiology, we investigate the biophysical properties that distinguish VDAC2 from VDAC1 and VDAC3. Unlike the latter, VDAC2 exhibits dynamic switching between multiple high-conductance, anion-selective substates. Using α-synuclein (αSyn)—a known VDAC1 cytosolic regulator—we found that higher-conductance substates correlate with increased on-rates of αSyn-VDAC2 interaction but shorter blockage times, maintaining a consistent equilibrium constant across all substates. This suggests that αSyn detects VDAC2's dynamic structural variations before final binding. We explored the dependence of VDAC2's unique amino-terminal extension and cysteines on substate behavior, finding that both structural elements modulate substate occurrence. The discovered conformational flexibility enables VDAC2 recognition by diverse binding partners, explaining its critical physiological role via dynamical adaptation to mitochondrial metabolic conditions.

INTRODUCTION

The voltage-dependent anion channel (VDAC) is the most abundant protein in the mitochondrial outer membrane (MOM), which represents a class of β barrel channels originally derived from the endosymbiotic bacterial ancestors of modern mitochondria. It is the major pathway for water-soluble metabolites and small ions to cross the MOM. In mammals, there are three VDAC isoforms: VDAC1, VDAC2, and VDAC3. Despite ~70% sequence similarity between the isoforms and the ability of them all to form large conductive anionic channels (~4 nS in 1 M KCl at room temperature), which gate in response to the applied voltage when reconstituted into a planar lipid membrane (PLM), each VDAC isoform has a distinct physiologic role. VDAC1 and VDAC2 are the most abundant isoforms, with VDAC3 expressed in low levels (~10% of the total VDACs) in most tissues, except in the testis (*1*, *2*). VDAC2 is the most expressed isoform in brain tissue, as well as in the placental endothelium (*3*). Studies in mice demonstrate that VDAC1 or VDAC3 knockouts are not lethal but result in metabolic impairment in the case of VDAC1 (*4*) and male infertility in the case of VDAC3 knockouts (*5*). VDAC2 knockout results in embryonic lethality or severely diseased neonatal pups (*6*, *7*). VDAC2 alone has been shown to regulate the B cell lymphoma 2 antagonist/killer (BAK)/B cell lymphoma 2–associated X protein (BAX)–dependent apoptosis pathways, rationalizing the results of the murine studies (*6*–*8*). In this paradigm, apart from its channel activity, VDAC2 acts as a membrane anchor for BAK/BAX within the MOM. In the case of BAK, binding to VDAC2 impairs its oligomerization in the MOM and subsequent apoptosis via cytochrome c release (*6*, *9*). While the human VDAC2 (hVDAC2) structure had eluded structural determination, the structure of hVDAC2 was recently identified as part of a supercomplex necessary for stabilizing the Parkinson's disease (PD)–related ubiquitin kinase PINK1 (*10*). In this role, VDAC2 formed a dimer mediated by disulfide bonds that tethers translocase of outer mitochondrial membrane 40 (TOM40) channels together so that PINK1, trapped in TOM40, can dimerize and trans-autophosphorylate. This unexpected finding suggests that VDAC2 may play a central role in mitophagy and PD etiology. VDAC2 differs from VDAC1 most obviously in an 11-residue N-terminal extension (NTE) and the presence of nine cysteines compared to two in VDAC1 (*11*). A mutagenesis study by Naghdi *et al.* (*8*) showed that neither the NTE nor the extra cysteines were essential for the VDAC2-BAK interaction, instead finding that a cytosol-facing loop connecting two β strands was the site of the interaction. Biophysical studies on VDAC2 have demonstrated that the NTE was important for maintaining the stability of the channel, compensating for the increased number of cysteines (*12*). VDAC2 channel properties are superficially identical to VDAC1 (*12*–*15*); however, studies on VDAC2 electrophysiology have identified subtle, yet unexplored, differences. The first study, systemically comparing the channel properties of each VDAC isoform (*13*), found that VDAC2 conductance deviated from a unimodal Gaussian distribution characteristic for VDAC1 or VDAC3. The authors speculated that VDAC2 existed in at least two states with different anionic selectivities, a finding recapitulated in a more recent study (*15*). VDAC2 has been shown to be slightly more permeable to Ca^{2+} than VDAC1 (*16*). The structural features and physiologic role of these states remain unidentified.

VDACs are known to be regulated by cytosolic proteins, including α-synuclein (αSyn), an intrinsically disordered neuronal protein intimately associated with PD (*17*, *18*). The large aggregates and fibrils of αSyn found in Lewy bodies in the brains of patients with PD are a hallmark of PD (*19*). αSyn aggregation and oligomerization are associated with its increased expression in dopaminergic

[1]Eunice Kennedy Shriver National Institute of Child Health and Human Development, NIH, Bethesda, MD, USA. [2]Department of Biology and Biological Engineering, California Institute of Technology, Pasadena, CA, USA. [3]National Institute of Neurological Disorders and Stroke, NIH, Bethesda, MD, USA. [4]Institute of Atomic and Molecular Sciences, Academia Sinica, Taipei, Taiwan. [5]National Institute of Diabetes and Digestive and Kidney Diseases, NIH, Bethesda, MD, USA. [6]Department of Biological Sciences, Indian Institute of Science Education and Research, Bhopal, India.
*Corresponding author. Email: rostovtt@mail.nih.gov

neurons in PD and are generally considered to be pathological phenomena (*19*, *20*). However, the exact mechanism of αSyn-induced pathology remains mainly unknown. In particular, the role of monomeric αSyn continues to be poorly understood. αSyn was found to be associated with both mitochondrial membranes, causing impairment of the mitochondrial respiratory complexes (*21*–*23*), oxidative stress (*24*), and fission (*25*, *26*). At the MOM, monomeric αSyn interacts with VDAC [reviewed in (*27*)] and translocates through VDAC1 into the mitochondrial intermembrane space (IMS), as was shown in neuroblastoma and HeLa cells (*28*, *29*).

In vitro, monomeric αSyn at nanomolar concentrations induces voltage-dependent reversible blockages of reconstituted VDAC channel conductance, seen as rapid current fluctuations on the scale of 1 to 100 ms between the VDAC open and αSyn-blocked states with the residual conductance of ~0.4 of the open state (*30*). αSyn is a 140-residue polypeptide that consists of three well-defined domains: an N-terminal amphipathic membrane binding domain, a central nonpolar NAC domain, and a disordered highly negatively charged C-terminal domain (*31*). αSyn is essentially disordered in solutions, but upon binding to the anionic lipid membranes, its N-terminal domain adopts different α-helical conformations while leaving the C terminus disordered above the membrane surface (*31*–*33*). On the basis of these structural data and the results of extensive kinetic analysis of VDAC interaction with αSyn at the single-channel level, the current model is that the N-terminal domain of αSyn remains membrane bound, and the anionic C-terminal domain is driven by the applied negative potential into the VDAC pore (*34*). At lower applied voltages, it retracts back to the same membrane surface after residing in the pore for some time, which depends on the voltage magnitude (*34*). The increasing negative voltage keeps the anionic C terminus inside the pore longer, which is seen as an exponential voltage dependence of the blockage time. The blocked state displays the reversal of selectivity, going to cationic versus anionic selectivity of the open state (*35*). At higher applied transmembrane voltages ($|V| > 35$ to 45 mV depending on experimental conditions), the blockage time starts to decrease with voltage, which is explained by αSyn translocation through the VDAC pore to the opposite side of the membrane (*30*). The translocation regime of αSyn was confirmed by direct experiments enabling real-time monitoring of a single αSyn molecule translocating through the VDAC pore (*35*).

In light of the proposed model, we can suggest a few immediate physiological implications of VDAC-αSyn interaction, driving regulation of adenosine 5′-triphosphate (ATP)/adenosine 5′-diphosphate (ADP) and Ca^{2+} fluxes across MOM. When the highly negatively charged C-terminal tail of αSyn is captured by the VDAC pore, it creates an electrostatic barrier for ATP/ADP (*36*) and, by inversing pore selectivity, promotes Ca^{2+} transport (*16*, *37*). The increased mitochondrial Ca^{2+} uptake in HeLa cells in response to αSyn overexpression (*38*) provides in vivo support to these predictions. Another anticipated implication of the proposed mechanism is the ability of αSyn to translocate through VDAC. Translocation of αSyn into the mitochondrial intermembrane space (IMS) was recently confirmed in neuroblastoma and HeLa cells (*28*, *29*). By entering mitochondria, αSyn could target electron transport chain complexes in the inner membrane, thus inducing mitochondrial dysfunction and eventually leading to cell death (*23*).

The cryo–electron microscopy structure of VDAC2 has recently been solved, which consists of 19 β strands and an α-helical N terminus lying in the middle of the pore (*10*). The position of NTE in VDAC2 remains unknown and was not observed in the cryo–electron microscopy density, suggesting that it is intrinsically disordered. Considering similar β barrels formed by all three VDAC isoforms and the proposed model of αSyn-VDAC interaction, one would expect a similar interaction of αSyn with all isoforms. However, it was found that the rate of αSyn capture by VDAC1 (the on-rate) is 100 times higher than that by VDAC3 (*39*), thus demonstrating, on a single-channel level, a clear quantitative difference between these two isoforms. Furthermore, the voltage required for αSyn to translocate through VDAC3 appeared to be 12 mV smaller than that for VDAC1 (*39*). These data enabled us to speculate that the difference in interaction with known, such as αSyn and dimeric tubulin, and still unidentified VDAC regulators could constitute a general mechanism that distinguishes isoforms in vivo (*40*). Therefore, we reasoned that VDAC2 may differ from the other two isoforms by its interaction with cytosolic regulator proteins, thus providing a biophysical basis for its unique physiological role.

In this study, we examine VDAC2's properties at the single-channel level. We use recombinant hVDAC2 wild type (WT) and its three mutants to understand the biophysical basis that distinguishes VDAC2 from the other two isoforms. We found that contrary to VDAC1 and VDAC3, which are characterized by a unique high-conductance or "open" state, VDAC2 is a dynamic channel that spontaneously switches between multiple high-conducting open substates that vary by conductance and occurrence while remaining anion selective—a defining feature of the ATP-permeable open states of VDAC. We show that monomeric αSyn induces similar characteristic blockage events in all VDAC2 open substates but with up to 10-fold different on-rates and blockage times. The higher on-rate of the αSyn-VDAC2 interaction always corresponds to the substate with the higher conductance when measured for the same single channel. However, the equilibrium constant of the αSyn-VDAC interaction, which accounts for both the on-rates and blockage times, remains the same for all substates, independent of their conductance. The finding that the pronounced difference is limited to the kinetic parameters only suggests that once the αSyn molecule is captured, its physical state and free energy in the pore are the same for all substates.

We propose that the appearance of distinct substates within the same channel and their different interaction kinetics with αSyn reveal the dynamic plasticity of VDAC2, which suggests a key for the explanation of the exceptional role of this multifaceted channel in the cell. The discovered conformational flexibility may allow VDAC2 to recognize a larger number of binding partners. These data could tentatively explain the physiological significance of VDAC2: its ability to dynamically adapt to metabolic cell conditions and change the rates of interaction with its multiple cytosolic protein partners.

RESULTS

VDAC2 dynamically switches between multiple high-conductance open substates

When reconstituted into PLMs formed from a mixture of dioleoylphosphatidylglycerol (PG):dioleoyl-phosphatidylcholine (PC):dioleoylphosphatidylethanolamine (PE) (2:1:1; w/w) in a symmetrical 1 M KCl solution, human recombinant VDAC2 WT forms channels with 3.0- to 4.0-nS conductance, which gate, i.e., transition from the high-conductance open state to the variety of low-conductance "closed" states in response to the applied voltage (Fig. 1, A and B).

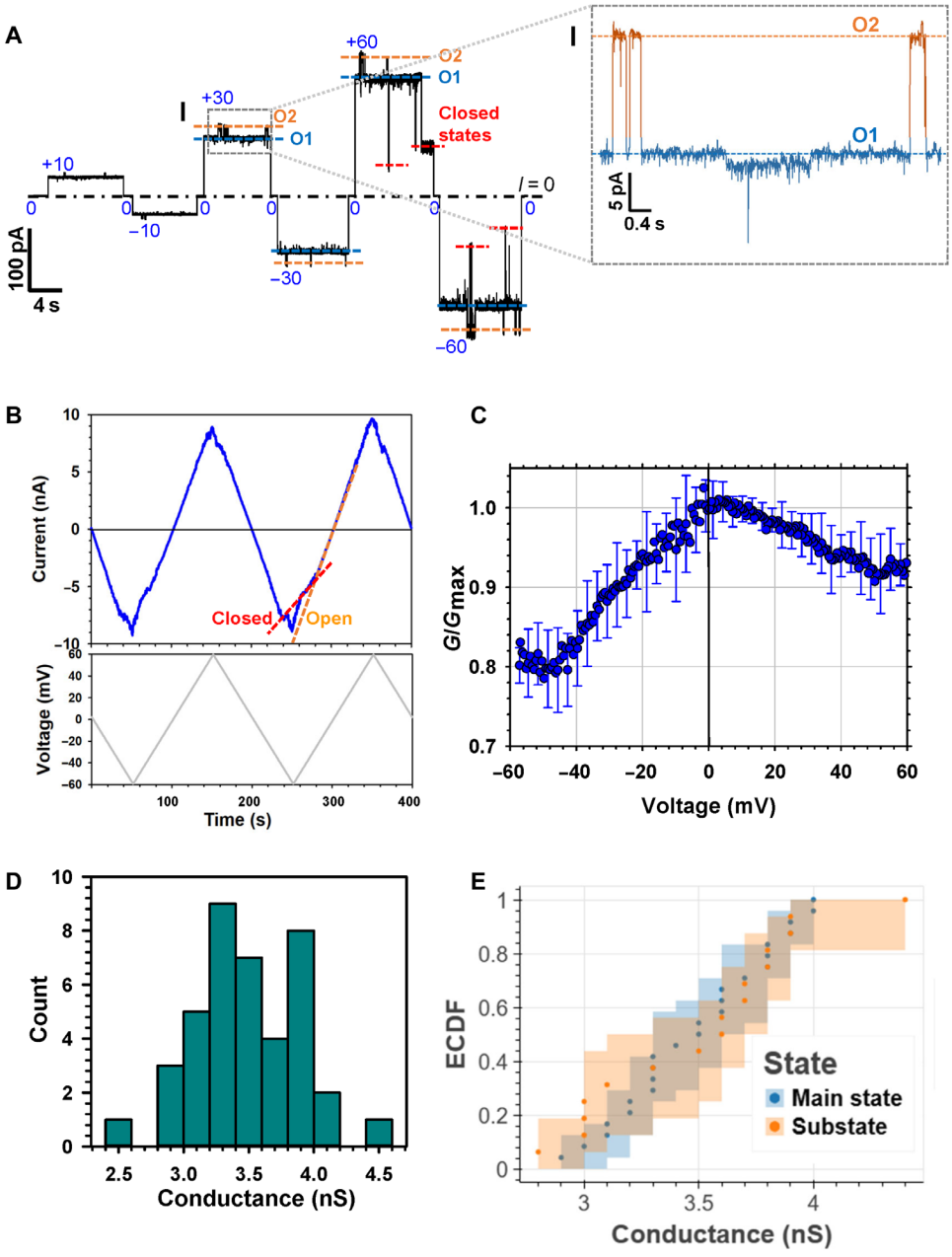

Fig. 1. VDAC2 stochastically switches between different "open" conductance substates. (**A**) Representative record of the current through a single VDAC2 WT channel reconstituted into the PLM formed from a 2PG/PC/PE lipid mixture in 1 M KCl (pH 7.4) at the increasing applied voltages. Two distinct substates of the open state ("O" state) indicated as O1 of 3.0 nS (blue dashed line) and O2 of 3.5 nS (orange dashed line) were observed at all voltages. Characteristic voltage gating behavior is seen at ±60 mV as stepwise current transition to a low-conductance, "closed" state (red dashed lines). Here and elsewhere, the dash-dotted line represents zero current; dashed lines indicate substates. The current record was digitally filtered at 500 Hz using a low-pass Bessel (eight-pole) filter. Inset (I): Transitions between two states are shown in a finer timescale using a digital 1-kHz Bessel filter. (**B**) Representative current trace obtained on a multichannel (~40 channels) membrane (upper panel) in response to the applied triangular voltage wave of ±60 mV and 5 mHz (bottom panel). Steep slopes at low potentials correspond to open states (orange dashed line), and reduced slopes at higher potentials indicate "closed" states (red dashed line). PLMs were made of polar lipid extract in 1 M KCl and 5 mM Hepes. (**C**) Voltage dependence of VDAC2 WT normalized conductance, G/G_{max}, obtained in multichannel experiments as in (B). G is the conductance at given voltage, and G_{max} is the maximum conductance at $|V| \leq 10$ mV. Data points are the means of three experiments ± SD. (**D**) VDAC2 WT single-channel conductance histogram. The main state conductance was measured for 24 independent molecules. (**E**) ECDF calculated for all main state (blue) and substate (orange) conductances observed in all experiments (n = 24 channels). Solid dots denote raw data points. The shaded region represents the 95% confidence interval from 10,000 bootstrap replicates.

This constitutes typical VDAC1 behavior (*41*, *42*). We examined VDAC2 gating in single-channel (Fig. 1A) and multichannel membranes (Fig. 1B) to find that the application of 50 to 60 mV was required to observe typical voltage gating (Fig. 1A) (*42*). The normalized conductance (G/G_{max}) plots for VDAC2 display the characteristic bell-shaped voltage dependence for all VDACs with enhanced gating, i.e., lower G_{min}, in response to negative applied voltages (Fig. 1C).

The notable difference that we found between VDAC2 and VDAC1 was the appearance of multiple high-conducting open states. They were evident at any applied voltages starting at 10 mV (fig. S1, A and B) in ~50% of single VDAC2 channels during an observation time of at least 20 min. The example of such spontaneous transitions between two high-conductance states can be seen in inset I in Fig. 1A of the single-channel record of the current through VDAC2. Conductance fluctuates between the long-lasting state O1 of 3.0 nS (indicated by blue dashed lines in Fig. 1A, I) and the short-lived state of 3.5 nS (indicated by the orange dashed line). On different single channels (in different PLMs), such substates were observed either for relatively short times, less than 10% of the time spent in the initial state, as shown in the representative trace in Fig. 1A, or for substantially longer times. The existence of multiple substates in VDAC2 results in a relatively wide distribution of open states' conductances, spanning the range from 3.0 to 4.0 nS (Fig. 1D). Other channels showed a single stable open state throughout the observation time (fig. S1A). To determine whether substate conductance distribution depends on the initial state in which the channel inserted in, we generated the empirical cumulative distribution function (ECDF) plots for the initially observed conductance states (main state, blue) and for the substates (substates, orange) (Fig. 1E). It shows that substate conductance distribution does not depend on the original state in which the channel inserts (main state in Fig. 1E). This suggests that a given VDAC2 channel can initially insert into PLM at any state and then subsequently spontaneously switch to a state with a different conductance.

High-conductance VDAC2 substates are anion selective

VDAC1 is known to have multiple voltage-induced "closed" conducting states, which are characterized by a wide range of conductances and low-anionic or cationic selectivity (*43*). This is in contrast with the unique anion-selective open state of VDAC1. To determine whether the observed high-conductance substates of VDAC2 can be reliably attributed to open states and are not voltage-gated states, we examined their selectivity. For this purpose, single channels were reconstituted in a 5× salt gradient (1 M KCl cis and 0.2 M KCl), where they displayed the same substate behavior as observed under symmetrical salt conditions. A representative trace of VDAC2 obtained in the salt gradient (Fig. 2A) shows two conducting states: the initial long-lasting state O1 (indicated by blue dashed lines) and the higher-conductance short-lasting state O2 (indicated by orange dashed lines) (inset I in Fig. 2A). In the salt gradient, substates can be observed at an applied voltage of 0 mV, indicating that their presence is voltage independent. The corresponding I/V (current versus voltage) plots for two states O1 and O2 are given in Fig. 2B. The linear regressions determine the slope (conductance) and the reversal potential (Ψ_R, the voltage corresponding to zero current) for each substate. Under these salt gradient conditions, positive Ψ_R indicates anionic selectivity, and negative Ψ_R indicates cationic selectivity. Both conducting substates proved to be anion selective. Moreover, the lower-conductance substate O1 has a higher reversal potential of 7.2 mV and, accordingly, higher anion selectivity than the higher-conductance substate O2 with $\Psi_R = 4.4$ mV (Fig. 2B).

The scatterplot of Ψ_R versus conductance for all observed conducting substates obtained in 19 individual VDAC2 WT channels is shown in Fig. 2C. Ψ_R is plotted as a function of conductance for the initial or main states (shown as blue circles), which are also typically the most probable states observed for a given channel, and for substates (shown as orange stars). The main states and substates could be clustered in at least two groups: one with higher conductance (>1.6 nS) and lower reversal potential and another with lower conductance (<1.6 nS, highlighted in haze blue) and higher Ψ_R (Fig. 2C). It could be seen that substates and main states of the channel occupy the same Ψ_R versus conductance clusters. To empirically determine the validity of such clustering, we performed *K*-means clustering analysis, with the cluster size determined by the maximum silhouette score. The analysis returned three clusters with the higher-conducting >1.6-nS states clustering in two groups and most of the low-conducting <1.6-nS states falling into a third cluster (fig. S1C).

These results suggest that the observed substates represent a set of VDAC2 open states characterized by anion selectivity. A comparison of VDAC2 selectivity with VDAC1 and VDAC3 confirms this conclusion. In Fig. 2D, it can be seen that the high-conductance state of VDAC2 (G_{high}, which corresponds to typical ~3.8-nS conductance in 1 M KCl symmetrical solution) is similar in conductance and anion selectivity (with a Cl^--to-K^+ permeability ratio $P_{Cl-}/P_{K+} \sim 1.4$) to the open states of VDAC1 and VDAC3, while the lower-conductance VDAC2 state (G_{low}, corresponding to ~3.1 nS in 1 M KCl) is characterized by slightly higher anion selectivity with $P_{Cl-}/P_{K+} \sim 1.5$.

VDAC2 open substates vary in the kinetics of their interaction with the cytosolic regulator αSyn

Previous work demonstrated that while the basic channel properties of VDAC1 and VDAC3 isoforms, such as conductance, ion selectivity, and voltage gating, are similar, their interaction with VDAC cytosolic protein partners—dimeric tubulin and αSyn—is markedly different, thus reliably distinguishing each isoform (*39*). Following these results, we tested the interaction between reconstituted hVDAC2 WT and αSyn at the single-channel level. According to the previously proposed model of αSyn-VDAC complexation (*44*), the first step of αSyn capture by the VDAC pore is binding of the αSyn N-terminal domain to the membrane surface (*34*, *45*) where αSyn preferentially binds to anionic lipids, as have been shown in multiple studies (*31*–*33*, *46*, *47*). Therefore, to maximize the αSyn-VDAC interaction, we used PLM formed from the 2PG/PC/PE lipid mixture. The 50% content of anionic PG in the lipid mixture increases the on-rate of αSyn-VDAC interaction, allowing for the faster acquisition of statistically reliable data (*45*). In addition, another advantage of using PLM of this lipid composition is that VDAC stays mostly open at the applied voltages of up to 60 mV (Fig. 1) (*42*), thus allowing the measurement of αSyn-VDAC interaction at the wide range of applied voltages. Figure 3A shows a representative trace of VDAC2 WT in the presence of αSyn. Initially, this channel showed two conductance levels, O1 of 3.0 nS and O2 of 3.6 nS, which were recorded at the applied voltages as low as 10 mV. Ten minutes after insertion, the channel spontaneously converted to a state with stable 3.8-nS conductance referred to as O3 (Fig. 3A, insets I and II). In all three states, the channel is blocked by αSyn, which is manifested by fast current transitions

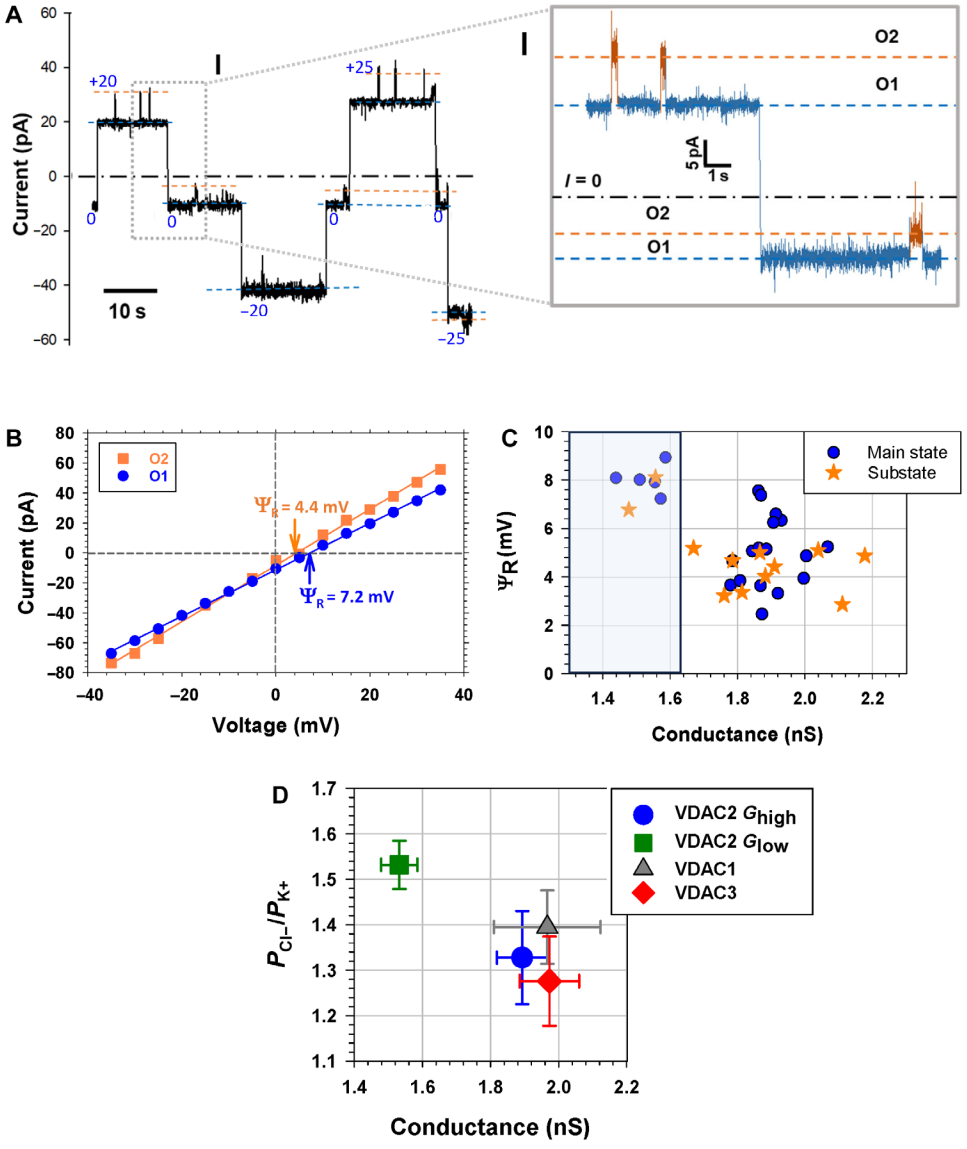

Fig. 2. VDAC2 substates are anion-selective open states. (**A**) A representative single-channel trace of the current through VDAC2 WT was obtained using a 1.0 M (cis)/0.2 M (trans) KCl gradient at different applied voltages, as specified. Blue and orange dashed lines indicate two open substates. Inset (I) shows a fragment of ion current (accentuated by a gray box) at a finer timescale, demonstrating two open states, O1 and O2, at the applied voltages of +20 and 0 mV. The current record was digitally filtered using a 500-Hz [1 kHz in (I)] low-pass Bessel (eight-pole) filter. Other experimental conditions were as in Fig. 1. (**B**) Current/voltage (*I*/*V*) curves were obtained for the two states O1 (blue circles) and O2 (orange squares) for the experiment shown in (A). Linear regressions allow for the calculation of the reversal potential (Ψ_R) indicated by arrows for each state. Positive Ψ_R corresponds to anion selectivity. (**C**) Reversal potential (Ψ_R) versus conductance scatterplot for all observed conductance substates: main or long-lasting (blue circles) and short-lasting (orange stars) substates for 19 individual VDAC2 WT channels. (**D**) Comparison of the mean open-state conductance and Cl^-/K^+ permeability ratio (P_{Cl-}/P_{K+}) for each VDAC isoform. The full set of the analyzed VDAC2 conductances was divided into a high-conductance state of >1.6 nS (G_{high}) and P_{Cl-}/P_{K+} ~ 1.3 similar to those of VDAC1 and VDAC3 and a state with a conductance lower than 1.6 nS (G_{low}) [highlighted by blue in (C)] and high anion selectivity with P_{Cl-}/P_{K+} ~ 1.5. Error bars are ±SD from at least five independent channel measurements for each VDAC isoform.

between one of the open states (O1, O2, or O3) and the corresponding blocked states, B1, B2, or B3, with ~0.4 conductance of the corresponding open state (Fig. 3A, insets I and II). Notably, αSyn does not block the VDAC2 voltage-induced low-conductance closed state (fig. S2), as was also reported for VDAC1 (*30*), because of its cationic selectivity. This is another piece of evidence indicating that high-conductance VDAC2 substates are substantially different from the voltage-induced "closed" states of the same single channel.

The important feature of VDAC2's interaction with αSyn is that the frequency of blockage events varies markedly between the high-conductance substates, which can be clearly seen in insets I and II in Fig. 3A with a higher time resolution. Notably, at the same applied voltage, the state with a higher conductance, O3, for a channel shown in Fig. 3A has a higher frequency of blockage events than the state with a lower conductance, O1. To quantify the αSyn-VDAC interaction, we plot the open times, τ_{on}, the time between

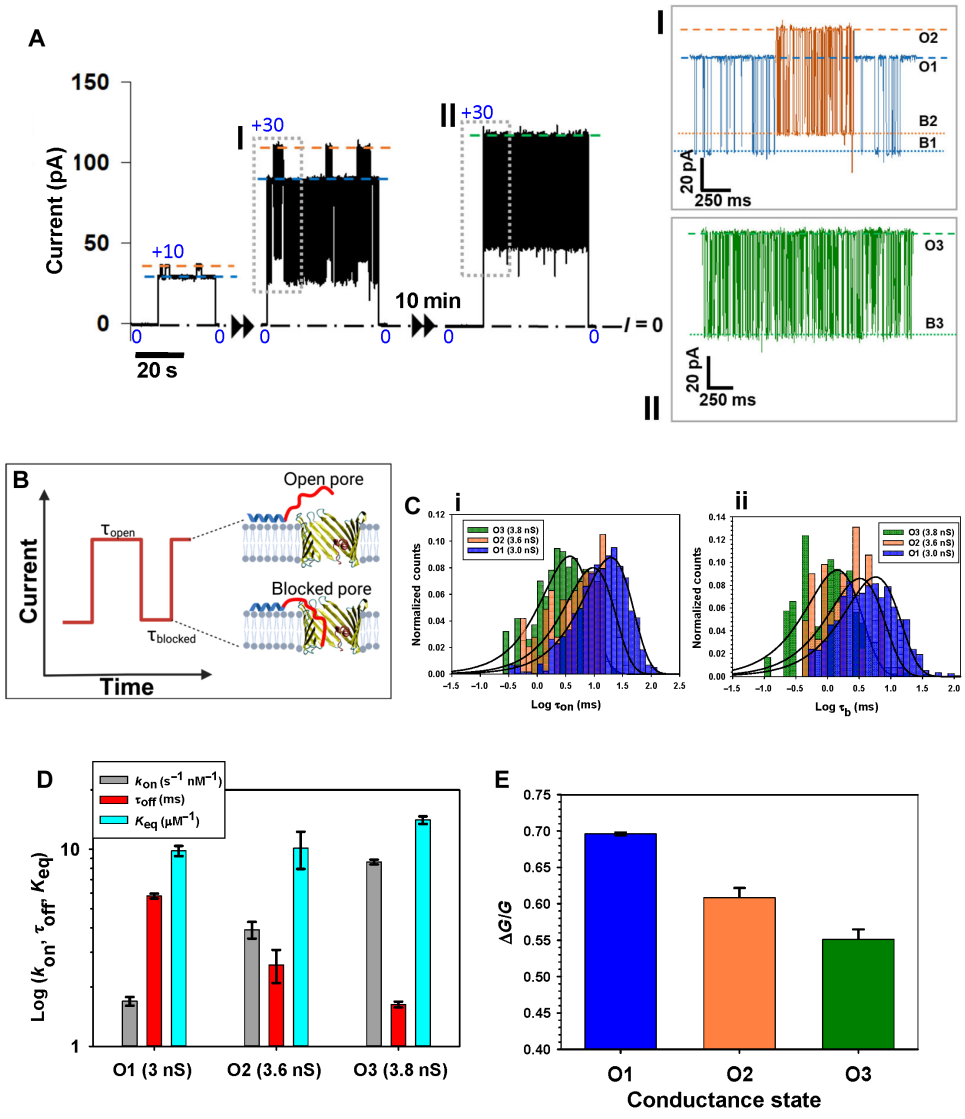

Fig. 3. VDAC2 dynamic substates differ from each other in their interaction with the cytosolic regulator αSyn. (**A**) Representative current record of a single VDAC2 WT channel in the presence of 10 nM αSyn, displaying robust substate behavior manifested as spontaneous fluctuations between the low-conductance (3 nS) long-lasting (O1) and high-conductance (3.6 nS) short-lasting (O2) substates at 10 and 30 mV. After 10 min, spontaneous transition to a higher-conductance (3.8 nS) substate (O3) is observed. Insets (I) and (II) show αSyn-induced blockage events at a finer timescale for each of the three substates at 30 mV (gray boxes). Open states (O1, O2, and O3) are indicated by dashed lines, and αSyn-blocked states (B1, B2, and B3) are indicated by dotted lines. (**B**) The cartoon illustrating the αSyn-VDAC interaction events is characterized by the time when the channel is open (τ_{on}) and the blockage time (τ_b), the duration of each blockage event. (**C**) Representative log-binned histograms of τ_{on} [(C), i] and τ_b [(C), ii] of each state at 30 mV obtained from the experiment in (A). Solid lines are fits to a single-exponential function with characteristic times $<\tau_{on}>$ equal to 19.7, 8.62, and 3.87 ms for states O1, O2, and O3, respectively [(C), i]; and $\tau_{off} = <\tau_b>$ equal to 5.79, 2.59, and 1.63 ms for states B1, B2, and B3, respectively [(C), ii]. (**D**) Comparison of kinetic parameters: $k_{on} = 1/(<\tau_{on}>[C])$, where $[C]$ is the αSyn bulk concentration, τ_{off}, and the equilibrium constant, $K_{eq} = k_{on}\tau_{off}$, of αSyn-VDAC binding for each state at 30 mV. Error bars are ±SD of three fitting algorithms for the exponential fits. (**E**) Comparison of αSyn-blocked conductance of each conducting state. $\Delta G/G$ is the relative conductance drop, where ΔG is the difference between open-state (G) and blocked-state conductances of states O1, O2, and O3. Error bars are ±SD between measurements of $\Delta G/G$.

consequent αSyn blockage events, and blockage times, τ_b (see cartoon in Fig. 3B), in log-binned histograms for each state at the applied voltage of +30 mV (Fig. 3C). State O1 has the longest intervals between αSyn blockage events, followed by O2 and, lastly, O3, demonstrating that τ_{on} decreases with the state's conductance increase (Fig. 3Ci). The blockage times follow the opposite sequence: State O1 has the longest $\tau_{off} = <\tau_b>$, followed by O2 and O3 (Fig. 3Cii). The comparison of the kinetic parameters of αSyn-VDAC binding for each state obtained in the experiment in Fig. 3A is shown in Fig. 3D. The on-rate constant of αSyn capture by the pore, $k_{on} = 1/(<\tau_{on}>[C])$, where $[C]$ is the αSyn bulk concentration, and the characteristic off-rate, τ_{off}, were calculated by averaging the rates determined via three separate fitting algorithms for the log-probability distribution (Fig. 3C) (see Materials and Methods). As conductance increases from state O1 to O2 to O3, k_{on} increases from 1.70 to 3.90 to 8.62 s^{-1} nM^{-1}, respectively, and τ_{off} decreases from 5.79 ms in O1

to 2.59 ms in O2 to 1.63 ms in O3. The equilibrium constant, $K_{eq} = k_{on}\tau_{off}$ (light blue bars in Fig. 3D), varies negligibly between the substates. To compare the trend in k_{on} values across multiple substates in individual VDAC2 channels, we plotted k_{on} values versus corresponding conductance (fig. S3A). In every case (seven independent experiments with different channels and a total of 12 analyzed substates), as substate conductance increased, k_{on} also increased (fig. S3C), confirming the results obtained on the same channel (Fig. 3D). This trend is consistent across multiple observed single-channel measurements despite large variability in absolute values of the kinetic parameters between individual channels and, correspondingly, a low coefficient of determination $R^2 = 0.33$.

For VDAC1 and VDAC3, the conductance of the αSyn-blocked state is ~0.4 of the open-state conductance (*30*, *39*), giving $\Delta G/G \sim 0.6$. A comparison of the blocked state's relative conductance, $\Delta G/G$, for states O1, O2, and O3 (as in Fig. 3A) is shown in Fig. 3E. State O1 has the highest $\Delta G/G$ with 0.70 of conductance blocked, followed by O2 with 0.61 and O3 with 0.55. A comparison of $\Delta G/G$ values across different substates using the same set of individual VDAC2 channels as for k_{on} and τ_{off} analysis confirms the trend found for the same channel (fig. S3D). Statistical analysis of the substates was performed using the nonparametric paired Wilcoxon signed-rank test, comparing substates observed on the same channel, allowing comparison between data taken at different voltages (fig. S3, A and B).

VDAC2 has a lower average k_{on} of αSyn blockage than VDAC1 but a larger variance (fig. S4A). At negative applied voltages, the ratio between the highest k_{on} and the lowest one is up to approximately three times. At positive applied voltages, there is an even larger variability between channels, namely up to ~10 times difference in k_{on} between different channels, reflecting the intrinsic asymmetry of the VDAC channel (*48*). Nevertheless, the range of k_{on} values for VDAC2 is below those for VDAC1 obtained under the same conditions (*45*).

VDAC2 NTE and extra cysteines affect the occurrence of conductance substates but do not eliminate them

VDAC2 differs most prominently from VDAC1 by the presence of an extra 11–amino acid NTE and 7 extra cysteine residues, 6 of which face the IMS in mitochondria (Fig. 4A) (*11*, *49*). These features have been proposed to contribute to VDAC2's unique function (*12*, *50*) and have already been shown to alter the chemical-physical properties of hVDAC2. Maurya and Mahalakshmi (*51*) showed that cysteine-less hVDAC2 protein has higher thermostability and, consequently, a more stable β barrel than the WT. They also showed that the 11-residue NTE plays a role in hVDAC2 refolding in micelles and lipids. However, neither cysteines nor NTE considerably affect VDAC2 basic properties such as single-channel conductance or voltage gating. On the basis of these data, we decided to determine whether these sequence features are responsible for VDAC2's dynamic substate behavior. We used two previously characterized constructs: hVDAC2 with truncated N terminus 1 to 11 residues (ΔN-VDAC2) and a mutant lacking all cysteines (VDAC2-ΔCys). Both ΔN-VDAC2 and VDAC2-ΔCys mutants reconstituted into the same 2PG/PC/PE PLM display channels with 3.8- to 4.0-nS conductance. However, lower-conductance states were still observed, prevalently in the ΔN-VDAC2 mutant and less so in the VDAC2-ΔCys mutant.

To compare substate occurrence between two mutants and VDAC2 WT, we calculated the ECDF for two mutants and the VDAC2 WT (Fig. 4B). This allows us to directly compare proportions of channels observed with substates. The analysis shows that ~93% of ΔN-VDAC2 channels have substates in comparison with ~54% of VDAC2 WT and ~19% of VDAC2-ΔCys channels (Fig. 4C). Thus, the removal of the first 11 amino acids greatly enhances substate occurrence. In contrast, the removal of cysteines reduces, although less extensively, the occurrence of substates. Neither mutation abolishes the occurrence of substates; therefore, these structural features of VDAC2 are not the source of substate appearance. However, the NTE and cysteines can allosterically regulate the dynamics of this behavior. The ΔN-VDAC2 channel is less thermostable than VDAC2 WT (*12*), while the VDAC2-ΔCys mutant had been shown to have a higher melting temperature (T_m) (*14*, *51*), thus suggesting that the presence of NTE and extra cysteines might influence the occurrence of the substates independently of their effect on β barrel thermostability.

NTE and cysteines affect the VDAC2 interaction with αSyn

We showed previously that the removal of cysteines from hVDAC3 altered that channel's interaction with αSyn (*39*). The on-rate of αSyn interaction with the VDAC3 cysteine-less mutant was ~10× higher than for the WT but only at negative potentials (*39*). Therefore, the next logical question was whether cysteines and NTE could affect VDAC2's interaction with αSyn. Both ΔN-VDAC2 and VDAC2-ΔCys mutants exhibited characteristic reversible blockages in the presence of αSyn (Fig. 5, A, C, and D). ΔN-VDAC2 displayed long-lasting substates with a visible difference in interaction kinetics with αSyn (Fig. 5A, inset I). The representative trace of a single ΔN-VDAC2 channel in Fig. 5A shows three substates, O1, O2, and O3, at the applied voltages of ±10 and ±35 mV. The ΔN-VDAC2 mutant exhibited two predominant long-lasting substates of 3.2 and 4.0 nS in different channels, allowing the measurements of the kinetic interaction with αSyn for both substates at the wide range of applied voltages on different single channels (Fig. 5B). As observed for VDAC2 WT (Fig. 3D), the higher-conductance substate of 4.0 nS has higher k_{on} than the lower-conductance substate of 3.2 nS at all voltages of both polarities (Fig. 5Bi).

The mean blockage time τ_{off} for VDAC2 mutants and the WT is also highly voltage dependent and has a characteristic biphasic behavior (Fig. 5Bii, and fig. S4B) as it was shown for VDAC1 and VDAC3 (*30*, *39*). At low applied voltages, τ_{off} increases with voltage, which corresponds to the blockage/retraction regime when an αSyn molecule is captured by the VDAC pore and then released back to the same side of the membrane (*34*, *35*, *52*). At higher applied voltages—usually $|V| > 40$ mV depending on the VDAC type and experimental conditions—τ_{off} decreases with voltage, corresponding to the translocation regime. This happens because, under the high applied voltage, the N terminus of αSyn detaches from the membrane, allowing the whole αSyn molecule to translocate to the opposite side of the membrane (*35*). The 4-nS substate of ΔN-VDAC2 has a shorter τ_{off} than the 3.2-nS substate at all applied voltages (Fig. 5Bii). This results in the unchanged equilibrium constant K_{eq}, calculated for the retraction regime only, which varies substantially between two substates across applied voltages (Fig. 5Biii), similar to the substates analyzed on the same VDAC2 WT channel (Fig. 3D). These results indicate that while substate transitions can reliably affect the kinetics of the αSyn-VDAC2 interaction, the final energy change or the affinity between αSyn and the VDAC2 pore remains unaltered.

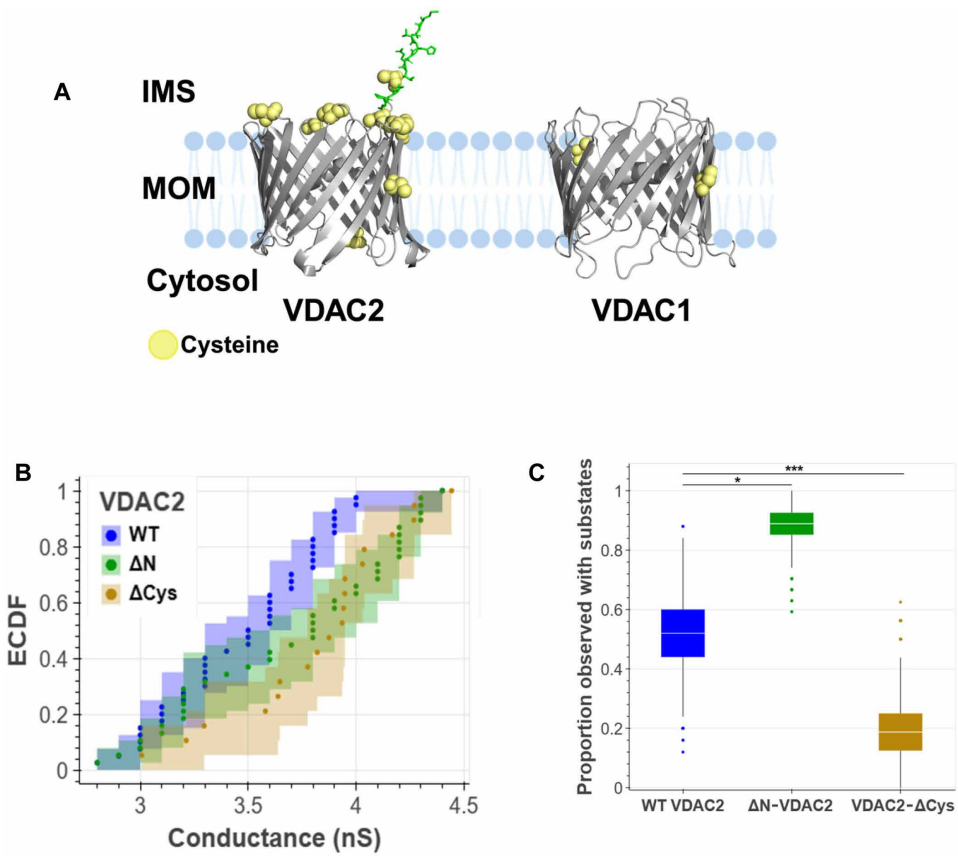

Fig. 4. NTE and cysteine mutations influence but do not abolish VDAC2 substates. (**A**) Structure of hVDAC2 (AlphaFold2 prediction) and VDAC1 (hVDAC1: Protein Data Bank ID: 2JK4). Cysteines are shown as yellow balls. The NTE of VDAC2 is shown in green. (**B**) ECDF was calculated using conductance values of the measured substates for all conductances observed for WT (blue), ΔN (green), and ΔCys (goldenrod) VDAC2 channels. Occurrence was liberally defined as whether a state transition had been observed during the entire recording period for a given channel. Of 24 single-channel recordings of VDAC2 WT, 13 channels displayed substate behavior compared to 25 channels of a total of 27 for ΔN-VDAC2 channels and 3 of 16 channels of VDAC2-ΔCys. Solid dots represent raw data points. The shaded region represents the 95% confidence interval from 1000 bootstrap replicates. (**C**) Box-and-whisker plots for the MLE probability of the binomial coefficient; substate behavior being observed in VDAC2 WT (blue), ΔN-VDAC2 (green), and VDAC2-ΔCys (goldenrod) channels. A total of 10,000 bootstrapped replicates was simulated from an MLE of the binomial coefficient originally calculated from 25, 27, and 16 observations of VDAC2 WT, ΔN-VDAC2, and VDAC2-ΔCys, respectively. The top and bottom of the box are, respectively, the 75th and 25th percentiles of the data. The line in the middle of the box is the median. The top whisker extends to the maximum of the set of data points that are less than 1.5 times the interquartile regions beyond the top of the box, with an analogous definition for the lower whisker. Data points not between the ends of the whiskers are plotted as individual points. Substate occurrence between mutants was compared with a chi-square test. *$P < 0.05$ and ***$P < 0.001$.

The VDAC2-ΔCys mutant also exhibited conductance substates but less frequently than ΔN-VDAC2 and the WT (Fig. 4C). An example of two substates in VDAC2-ΔCys channel of 3.0 and 3.5 nS is shown in Fig. 5D. The on-rate of αSyn blockages was again higher in the higher-conductance substate than in the lower-conductance one. Notably, the conductance of this predominant state is typical for the open-state conductance of VDAC1.

E84A mutation increases the β barrel thermostability of VDAC2 but does not abolish the substates

One of the differences between mammalian VDAC isoforms is the charged glutamate in position 73 in VDAC1 and position 84 in VDAC2 and a noncharged glutamine in position 73 in VDAC3 (*53*). The E84 residue in VDAC2 corresponds to the notorious E73 of VDAC1—a charged residue buried in the middle of the hydrophobic membrane and continuously under investigation to determine its physiological relevance (*42*, *54*–*56*). E73 was implicated in the stability of the VDAC1 β barrel, whose dimeric channel interactions appear to be largely determined by this residue (*57*, *58*). Previous work on VDAC gating has demonstrated that β barrel dynamics are often the result of subtle allosteric network interactions across the channel (*59*). E84 in VDAC2 is thought to be involved in biologically relevant interactions such as those with ceramide (*60*). We hypothesized that if conductance substates are due to the dynamic rearrangement of the salt bridge ensemble inside the pore, leading to the set of pores of different selectivities and conductances, it is natural to expect a notable involvement of the E84 residue. Following this hypothesis, we tested the possible involvement of this residue in conductance substate formation in VDAC2 by using VDAC2 mutant E84A, which replaces the membrane facing glutamate. E84A displayed enhanced thermostability, as measured by native tryptophan scanning fluorimetry (Fig. 6A). Its thermostability is substantially higher than that of VDAC1 and VDAC2, indicating the reduced flexibility of the β barrel. The similar effect of VDAC1

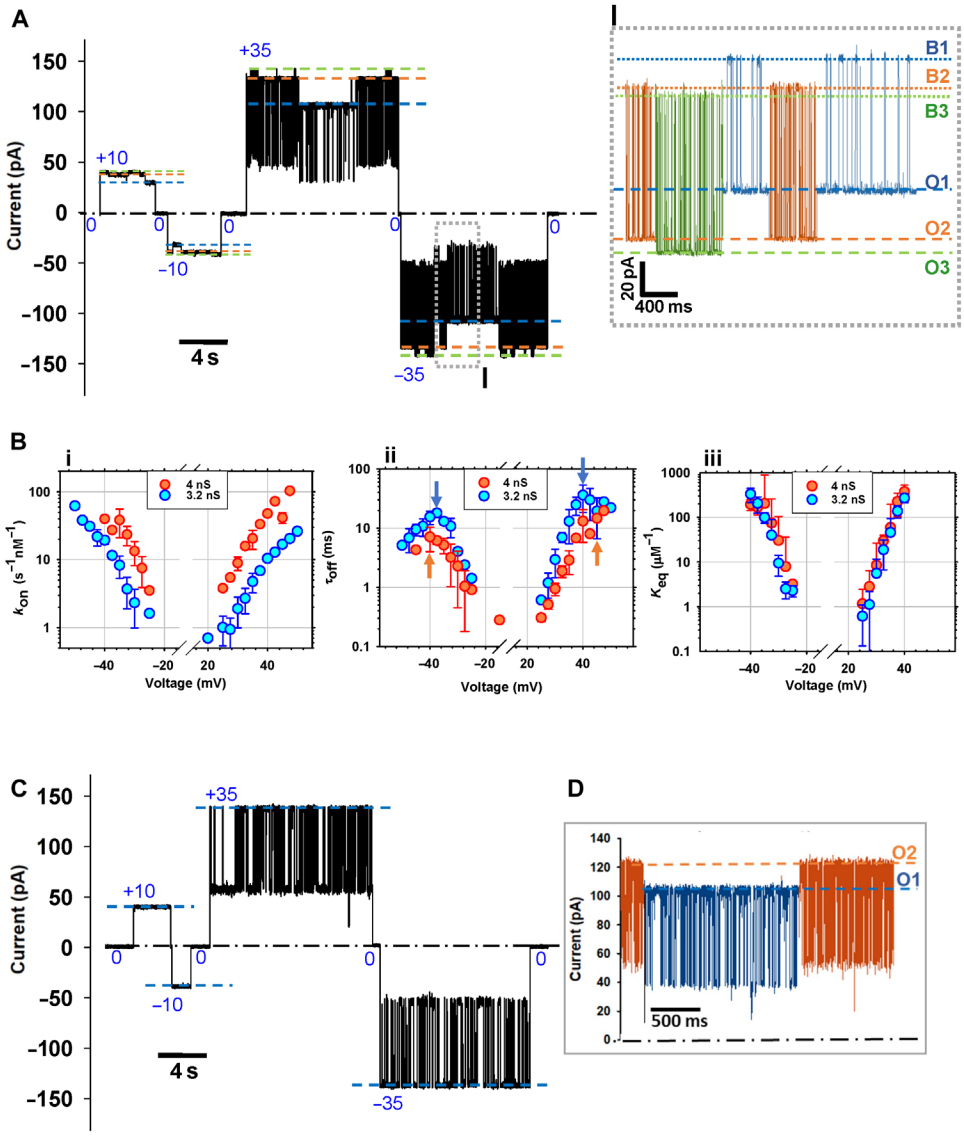

Fig. 5. αSyn blocks the higher-conductance substates with a higher on-rate than the lower-conductance states across VDAC2 mutants. (**A**) Representative single-channel current trace obtained with the reconstituted ΔN-VDAC2 mutant with 10 nM αSyn added to both sides of the membrane. Three distinct substates, O1, O2, and O3, are observed at ±10 and ±35 mV. Inset (I) shows αSyn-induced blockage events at a finer timescale for each of the three observed substates at −35 mV (accentuated by the gray box in the left trace). Open states O1, O2, and O3 can be observed along with their corresponding αSyn-blocked states B1, B2, and B3. The current record was digitally filtered using a 1-kHz low-pass Bessel (eight-pole) filter. (**B**) Voltage dependences of the on-rate constant k_{on} [(B), i], the mean blockage time τ_{off} [(B), ii], and the equilibrium constant K_{eq} [(B), iii] (calculated for the retraction regime only) of αSyn binding to two ΔN-VDAC2 substates with conductances of 4 and 3.2 nS. Arrows in [(B), ii] indicate the transitions between blockage/retraction and translocation regimes. Data are the means of three independent experiments ± SD. (**C**) Representative current record of the VDAC2-ΔCys single channel in the presence of 10 nM αSyn on both sides of the membrane showing one open state of 4 nS. (**D**) Example of the current record of VDAC2-ΔCys with two substates of 3.5 and 3 nS obtained at the applied voltage of +35 mV. Current records were digitally filtered using 500-Hz (C) and 1-kHz (D) low-pass Bessel (eight-pole) filters.

E73—the residue analogous to E84 in VDAC2—on VDAC1 dynamics has been shown by using the combination of solid nuclear magnetic resonance (NMR) spectroscopy and molecular dynamics simulations by Villinger *et al.* (*58*). The removal of the charge on E73 by either mutation or chemical modification reduced the motions of six VDAC1 N-terminal β strands underlying the key role of E73 in the elevated N-terminal protein dynamics.

However, notwithstanding the fact that the E84A mutant increased thermostability, the substates were still observed (Fig. 6B and fig. S5B). The VDAC2 E84A mutant gates similarly to the WT in single and multichannel experiments (fig. S5B). Thus, the E84 residue does not affect VDAC2 voltage gating, consistent with observations in the E73A VDAC1 mutant voltage gating experiments (*42*). The VDAC2 E84A mutant displayed more stable and long-lasting substates than the WT, similarly to the substate stabilization observed in ΔN-VDAC2. An example of the E84A mutant displaying two long-lasting stable substates of 3.0 and 3.6 nS is shown in Fig. 6B in the presence of 10 nM αSyn. Similar to VDAC2 WT and

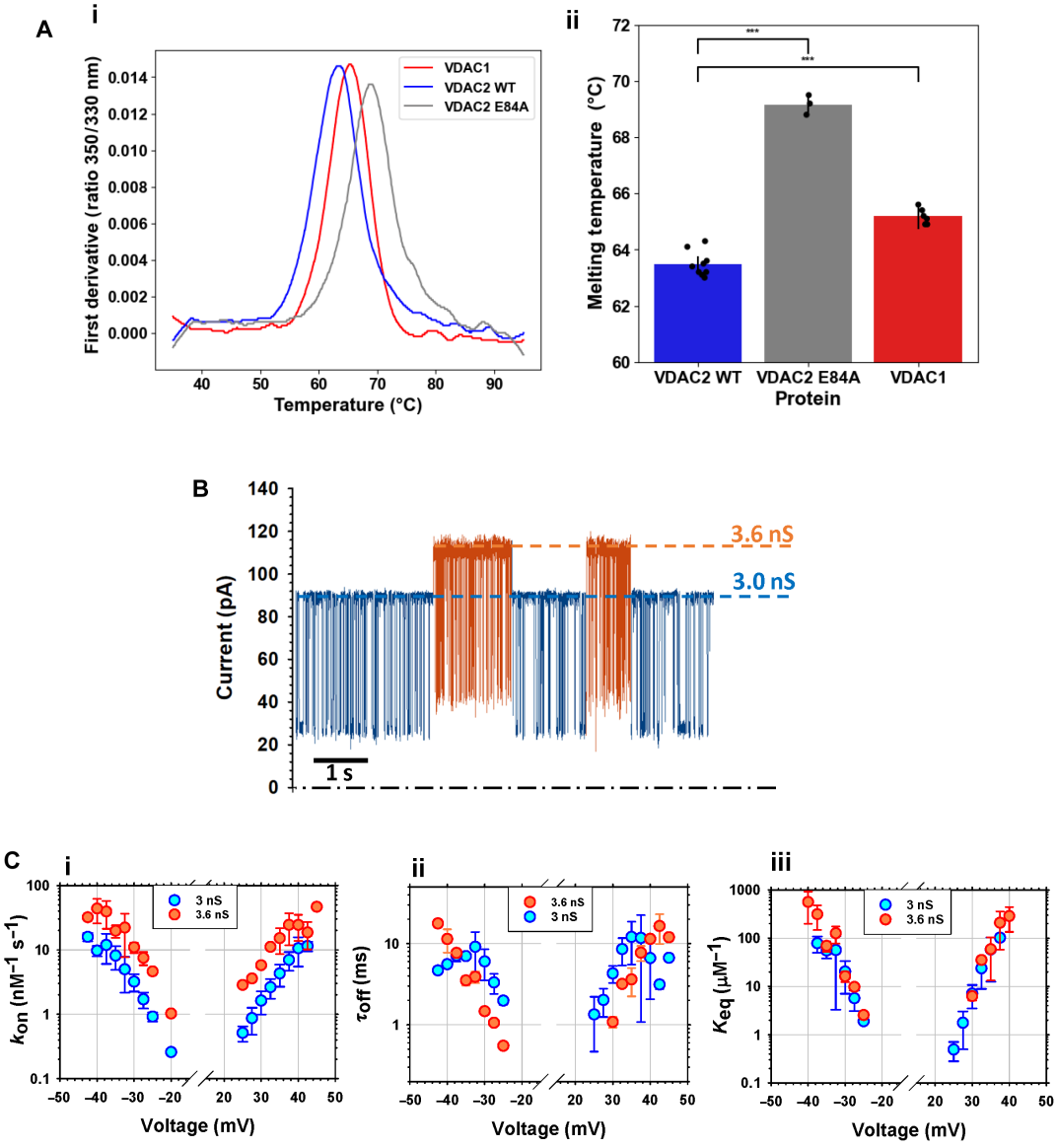

Fig. 6. The E84 residue of VDAC2 contributes to β barrel stability but does not affect the substate appearance. (**A**) [(A), i] The first derivative of the ratio of 350/330 nm tryptophan fluorescence versus temperature demonstrates the inflection melting point (T_m) for VDAC1 (red), VDAC2 WT (blue), and VDAC2 E84A (gray). [(A), ii] Box plot and scatterplot demonstrating average T_m for VDAC1 (red), VDAC2 WT (blue), and VDAC2 E84A (gray). Melting temperatures were compared with Student's *t* test; ***$P <$ 0.000001. (**B**) Representative current record of the VDAC2 E84A mutant showing two equally long-lasting conducting states of 3.0 and 3.6 nS in the presence of 10 nM αSyn on both sides of the membrane at the applied voltage of 30 mV. The current record was digitally filtered using a 1-kHz low-pass Bessel (eight-pole) filter. (**C**) Voltage dependences of the on-rate constant k_{on} [(C), i], the mean blockage time τ_{off} [(C), ii], and the equilibrium constant K_{eq} [(C), iii] of αSyn binding to two VDAC2 E84A states with conductances of 3.6 and 3.0 nS. Data are the means of three independent experiments ± SD.

the ΔN-VDAC2 and VDAC2-ΔCys mutants, the substate with a higher conductance of 3.6 nS in the E84A mutant has higher k_{on} and shorter τ_{off} than the lower-conductance substates of 3 nS, resulting in unchanged K_{eq} (Fig. 6C). These findings indicate that similarly to NTE and extra cysteines, E84 mutation affects β barrel flexibility but does not eliminate the substate appearance.

DISCUSSION

VDACs have been implicated in diverse mitochondrial signaling pathways, with VDAC2 being crucially important in development (*6*, *9*). Yet, the biophysical underpinnings of its special role in regulating functions remain unexplored. In this study, we revisited the basic biophysical properties of recombinant hVDAC2 using single-molecule electrophysiology to demonstrate the unique plasticity of this channel's properties and its interaction with cytosolic proteins. Our data show that VDAC2 stochastically switches between multiple high-conductance states, which results in a wide conductance distribution of the "open" state uncommon for other VDACs. The existence of VDAC2 multiple open states (but not the spontaneous transitions between them) was reported previously (*13*), with an average conductance of ~3.5 nS in 1 M KCl at room temperature,

which is lower than the typical open-state conductance of VDAC1 and VDAC3 under these conditions. We verified that these states are not the conventional VDAC's voltage-gated states because they are even more anion selective than typical ~4-nS open states of VDAC1 or VDAC3 (Fig. 2C) (*39*) as opposed to the more cationic voltage-gated states. Besides, they are observed at all applied voltages starting from as low as 10 mV with the frequency of their appearance independent of the applied voltage (Figs. 1 and 2), suggesting that membrane potential, including in vivo conditions, is not required to induce substate behavior. Under sufficiently high applied voltage, VDAC2 characteristically gates similarly to its other two isoforms (*39*, *42*) and to VDACs isolated from their native mitochondria of different species—fungus, yeast, or plant (*43*, *61*–*63*). This is manifested by a bell-shaped conductance versus voltage (*G*/*V*) dependence (Fig. 1C) and single-channel current transitions from the open state to the variety of closed states under the applied voltages of $|V| \geq 60$ mV (Fig. 1A). Therefore, the distinctiveness of VDAC2 among the three isoforms is that instead of the unique high-conductance anion-selective state, VDAC2 has a variety of such states. Notably, the characteristic duration and probability of each conductance state vary considerably between individual channels. The selectivity of the states with high conductances, which appeared to be in the range of open-state conductances of VDAC1 and VDAC3 (1.8 to 2.1 nS in a 1.0/0.2 M KCl salt gradient), fits into the range of VDAC1 and VDAC3 selectivity with a permeability ratio $P_{Cl-}/P_{K+} = 1.35 \pm 0.15$, while the VDAC2 substates with a lower conductance of 1.5 ± 0.05 nS have, on average, even higher anionic selectivity with $P_{Cl-}/P_{K+} = 1.5 \pm 0.05$ (Fig. 2D).

Using αSyn, a known potent cytosolic regulator of VDAC1 and VDAC3 (*16*, *28*, *39*), as a sensitive molecular probe of the VDAC pore, we explored different substates of VDAC2. We found that αSyn characteristically blocks all registered high-conductance VDAC2 substates. Notably, αSyn does not block conventional voltage-gated low-conductance states in either VDAC2 or other VDACs (*30*). This, together with anionic selectivity and high conductance, proves that these VDAC2 substates differ from the voltage-induced, more cation-selective lower-conductance states. Our results also show that αSyn quantitatively discriminates between different high-conductance states: The on-rate of αSyn capture by the VDAC2 pore rises with the substate conductance, while the blockage time decreases (Fig. 3D). This correlation is especially clear if the on- and off-rates for different substates are compared on the same VDAC2 WT channel. Across multiple individual channels of VDAC2, considerable variability in kinetic parameters exists, especially in k_{on} values, suggesting that the channel structure is highly dynamic. The enhanced conformational heterogeneity of VDAC2 in comparison with VDAC1 was suggested by Gattin *et al.* (*64*) based on broad solid-state NMR spectra obtained with VDAC2 in liposomes, indicating a large structural ensemble. The following solid-state NMR study of VDAC2 reconstituted in two-dimensional lipid bilayer crystals by Eddy *et al.* (*65*) showed that line shapes and peak dispersion exhibited by VDAC1 and VDAC2 are very similar and mostly depend on protein sample preparation. However, they also found that the extended N-terminal residues of VDAC2 were not sufficiently mobile on very fast timescales to be detectable in ^{13}C INEPT (insensitive nuclei enhancement by polarization transfer)–type experiments. In addition, these residues were not observable in their cross-polarization experiments, suggesting that the N-terminal tail is dynamic, possibly indicating conformational heterogeneity. These two structural studies testify to the difficulties of studying an enigmatic VDAC2 protein.

Considering that VDAC permeability to mitochondrial metabolites, such as ATP, ADP, and Ca^{2+}, depends on VDAC pore anion/cation selectivity, we can speculate that by switching between substates, VDAC2 is capable of fine tuning the regulation of metabolite and Ca^{2+} transport in and out of mitochondria (*40*). If such a physiologically meaningful mechanism exists, the immediate questions to answer concern the structural features of the substates' appearance and the physiological factors that regulate these substates in VDAC2 in live cells.

Possible conformational changes in VDAC2 leading to substate appearance

In an attempt to answer the first question, we studied the effect of the apparent sequence differences between VDAC2 and VDAC1—the 11–amino acid NTE and the seven extra cysteines—on the formation of substates. We found that both NTE and cysteines quantitatively affect substates' appearance frequencies (Fig. 4) with their substantial decrease in VDAC2-ΔCys down to ~19% and increase up to ~92% in ΔN-VDAC2 compared with ~54% of substates occurrence for the WT. The absence or presence of NTE and extra cysteines influences substates' appearance but does not eliminate them, thus suggesting that neither is the structural basis for substates' formation. Furthermore, the deletion of NTE stabilizes two predominant conductance substates in different ΔN-VDAC2 channels.

The VDAC2 E84A mutant is more thermostable than the VDAC2 WT and VDAC1 (Fig. 6A). Still, the reduced flexibility of its β barrel does not eliminate conductance substates. Like in ΔN-VDAC2, E84A mutation results in the stabilization of two predominant substates of 3 and 3.6 nS. The kinetic analysis of αSyn interaction with ΔN-VDAC2 and E84A mutants confirms the results obtained in VDAC2 WT. They also exhibit a positive correlation between conductance and k_{on} and a negative correlation between conductance and τ_{off}, resulting in the same K_{eq} for both conductance levels. The results show that VDAC2's NTE, cysteines, and E84 residue all contribute to, but are insufficient for, determining VDAC2's dynamic behavior. On the basis of the available structural and computational studies on VDAC1 (*57*–*59*, *66*, *67*) and the predicted structural similarity between VDAC1 and VDAC2 (*49*) shown experimentally for VDAC2 zebrafish (*68*), we can only speculate that the variety of conductance substates in VDAC2 may arise from dynamic rearrangements in the network of charged residues and salt bridges inside the pore in the proximity to the restriction zone and the tentative selectivity filter formed by two N-terminal α helices as in VDAC1 (*59*, *69*–*71*). The enhanced flexibility of the VDAC2 β barrel in comparison with VDAC1, manifested in its reduced thermostability (Fig. 6A), should also contribute to the proposed dynamicity of the salt bridges. The conductance substates were also observed for zebrafish VDAC2 (fig. S6). Furthermore, αSyn recognizes these substates by interacting from both sides of the bilayer, implying that the structural changes underlying the states' appearance most likely occur close to the center of the channel rather than in the asymmetric loops on either cytosolic- or mitochondrial-facing sides.

One of the important results is that despite the substantially different on-rates of αSyn capture by different VDAC2 substates, the equilibrium constants K_{eq} remain virtually unaltered. This can be explained by the transition path energy landscapes shown in Fig. 7 for two VDAC2 substates. K_{eq} is an exponential function of the

change in the free energy ΔU between the minima for the membrane-bound "free" αSyn molecule (potential well on the left) and for the pore-trapped one (potential well on the right). Because the experiment does not show any differences in the equilibrium constant in different substates, this means that ΔU is conserved, suggesting that the physical state of the αSyn molecule trapped within the VDAC pore is the same for all the substates. However, the profound changes in the on- and off-rates indicate that the region with the highest energy (the transition state) that the synuclein molecules must cross before reaching their final state in the pore differs for different substates. We can estimate the change in the transition state energy for substates (1) and (2), $\Delta\Delta U^{(1,2)}$, from k_{on} values as

$$\Delta\Delta U^{(1,2)} = k_B T \ln\left[\frac{k_{on}^{(1)}}{k_{on}^{(2)}}\right] \quad (1)$$

where $k_{on}^{(1)}$ and $k_{on}^{(2)}$ are the on-rates in substates (1) and (2), respectively. For example, applying Eq. 1 to the WT channel data presented in Fig. 3, we find that the change in the transition state energy between the open substate with the highest conductance, O3, and that with the lowest conductance, O1, is $1.6k_BT$.

On the one hand, empirical observations on αSyn-VDAC interaction (*30*, *45*) show that the on-rate is a strong exponential function of the applied voltage. On the other hand, in the case of open VDAC2 substates studied here, it turns out that the on-rate is very sensitive to the ionic current through the channel, even at the same applied voltage. Specifically, it increases up to an order of magnitude for the higher currents, corresponding to the substates of higher

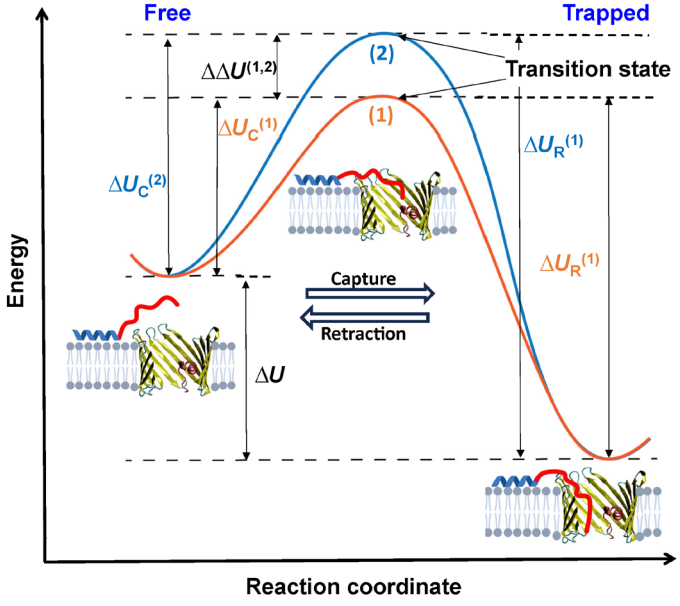

Fig. 7. Changes in the transition state energy barrier underlie the kinetic differences in the αSyn-VDAC interaction between substates. Free energy landscape diagram representing a model of the αSyn-VDAC interaction as a function of the reaction coordinate. The potential well of the initial state of free αSyn bound to the membrane is shown on the left. The potential well of the final state, whereupon the αSyn molecule is captured by the VDAC pore, is shown on the right. The energy landscape experienced by the αSyn molecule as it complexes with higher-conductance VDAC2 substate (1) is represented in orange, whereas the landscape for lower-conductance substate (2) is represented in blue.

conductance. In both scenarios—increasing applied voltage and increasing current at the same voltage—the fraction of the applied voltage that projects into the bulk solution in the vicinity of channel entrances increases. This is especially important in the case of VDAC because of the quite substantial access resistance of this channel, as was shown in experiments with water-soluble polymers that change the specific conductivity of the bulk solution (*72*, *73*) and confirmed within a mean-field approach by solving three-dimensional Poisson and Nernst-Planck equations (*74*). The fraction of the applied potential extending into the bulk changes the local concentration of charged molecules in the vicinity of the channel entrance and thus is able to change their capture rates. A similar phenomenon was described for DNA capture into nanofabricated solid-state nanopores (*75*) using the notions of "electrostatic focusing" and "effective capture radius" (*76*). A natural question is whether the field at the channel entrance is strong enough to account for the observed effects and contribute substantially to the free energy profile in Fig. 7.

Let us first analyze the on-rate voltage dependence presented in Figs. 5B and 6C. The total channel resistance, R, is the sum of access resistances at both entrances of the channel, $2R_{acc}$, and the resistance of the channel proper, R_{ch_p} (*77*)

$$R = 2R_{acc} + R_{ch\_p} \quad (2)$$

Both experimental work and the mean-field calculations performed for VDAC in 1 M KCl give the value of $2R_{acc}$ as 19 to 20% of the total channel resistance, that is, $2R_{acc} \simeq 0.2R$, which means that the access resistance at each channel entrance is close to $0.1R$. Therefore, ~10% of the applied voltage drops at the channel entrance. The data in Figs. 5B and 6C show that upon a 10-mV increase in the (modulus of) applied voltage, the k_{on} increases by a factor of ~8. Using Eq. 1 for $\Delta\Delta U^{(1,2)}$, where indices (1) and (2) now refer to the heights of the barriers for αSyn capture, ΔU_C, at the two voltages differing by 10 mV, we arrive to $1.7k_BT$. If we now assign the on-rate increase to the access resistance effect, then recalling that the change in the fraction of potential extending from the channel is 10% only, that is, $\Delta V_{acc} \simeq 1$ mV, and using

$$\Delta\Delta U^{(1,2)} = \Delta V_{acc} Q_{trap} \quad (3)$$

we arrive at ~50 elementary charges for the effective "trapping charge," Q_{trap}. This charge substantially exceeds the total charge of the αSyn C terminus, meaning that the applied voltage effect on the height of the transition state in Fig. 7 is more complex.

Let us now look at the change in the on-rates between the open substates using the same line of reasoning. As explained above, at 30 mV of applied potential, the transition of the VDAC2 channel from open substate O1 with a conductance $G^{(O1)} = 3.0$ nS to substate O3 with a conductance $G^{(O3)} = 3.8$ nS decreases the barrier by $1.6k_BT$. The change in the V_{acc} can be estimated through the change in the channel current, $\Delta I = \left(G^{(O3)} - G^{(O1)}\right)V$, as $\Delta V_{acc} = R_{acc}\Delta I = 0.65$ mV. Using Eq. 3, we arrive at the Q_{trap} of ~60 elementary charges. Again, this number is too large for the access resistance effects to explain the on-rate change between the states. However, the closeness of the two charge estimates, namely 50 versus 60, strongly suggests a similar physical mechanism of on-rate regulation in both cases. The capture is governed by the voltage distribution along the channel and within its access areas, which defines the physics of the observed phenomena. The exponential dependence of the on-rate

on voltage and a factor of four overestimation of Q_{trap}, compared to the actual charge of the αSyn C terminus, means that the capture of a disordered protein molecule by the channel is a complex process dominated by an entropic barrier (*78*) and that the transition state in Fig. 7 corresponds to the C terminus being partially captured by the pore. This way, the potential drop over the terminus is much larger than the potential drop over the VDAC access resistance.

The notable differences in $\Delta G / G$ found for different substates (Fig. 3D) also suggest that the substates should vary by structural rearrangements inside the pore. One may expect that the trapped polypeptide will influence the narrower, less conducting channel to a greater degree than the wider, more conducting one.

It is worth noting here that a similar correlation between the channel conductance and the on-rate of αSyn molecule capture was previously demonstrated when comparing three different β barrels formed by α-hemolysin, MspA, and VDAC (*44*). At the applied voltage of 35 mV, VDAC1, the channel with the highest conductance of 4 nS in 1 M KCl, has about three orders of magnitude higher on-rate than α-hemolysin, the channel with the lowest conductance of 0.73 nS in the same salt. However, the equilibrium constant was not conserved for these three channels, which is opposite to what is reported here for the VDAC2 substates. We conclude that the regulation of all substates of the open conformation of VDAC2 by αSyn is described by the same affinity, suggesting that once the αSyn molecule is captured, its physical state and interactions in the pore are the same for all substates but differ substantially by its kinetic parameters.

Physiological implications of VDAC2 unique plasticity

It has been recognized that the physiological roles of all three VDAC isoforms, and particularly VDAC2, exceed their function as "simple" pores (*79*, *80*). β Barrel pores are unique to the outer membrane of Gram-negative bacteria, mitochondria, and plastids, suggesting a common evolutionary origin (*81*). While the bacterial ancestor of VDAC is still unknown and controversial, VDAC is believed to share a common evolutionary origin with other 19 stranded β barrel channels in the MOM such as TOM40 and Mdm10 (*82*). One characteristic that distinguishes VDAC2 from the other isoforms is the NTE. In TOM40, the NTE, which is exposed to the mitochondrial IMS, physically interacts with other TOM complex members (*83*). It is likely that VDAC2's NTE also interacts in a similar fashion with other MOM and IMS proteins, thus defining VDAC2's physiological uniqueness among three isoforms (*79*). It would be of great importance to identify VDAC2-specific interactors using proximity labeling or immune precipitation mass spectrometry experiments. We can further speculate that by interacting with VDAC2 partner proteins, the N terminus could also, in turn, affect the state of VDAC2 conductance and, consequently, its selectivity, which defines VDAC's permeability for calcium (*16*, *84*) and ATP/ADP (*85*, *86*).

VDAC2 has two cysteines on the NTE along with the six cysteines on the loops facing IMS that may have a role in sensing oxidative stress in the IMS. Many studies and reviews have pointed to the nine cysteines of VDAC2 as being critical for its function (*12*, *14*, *50*, *51*, *87*, *88*). The strongest suppression of substate behavior was observed in the cysteine-null mutant VDAC2-ΔCys (Fig. 4C), suggesting that the redox state of mitochondria and oxidation states of the cysteines in VDAC2 could strongly affect the conformational state of the channel. While an extensive study highlights the important role of VDAC3, the isoform that has four cysteines facing the IMS, in redox signaling (*89*), there is a lack of studies on such a role of VDAC2. Our finding that VDAC2's cysteines modulate substate occurrence suggests that mitochondrial reactive oxygen species production could change the redox state of VDAC2, thereby transmitting the mitochondrial redox state to the cytoplasm.

The unexpected finding that substates vary by the kinetics of αSyn's interaction with VDAC2 but not its affinity implies that substates do not tune αSyn regulation of channel fluxes. However, the altered kinetics demonstrate that the capture of the synuclein molecule is affected by the structural changes in the channel. It is natural to expect that such conformational changes in VDAC2 will affect its interactions with other proteins. Potential interactors may include cytosolic pro-apoptotic proteins such as BAK and BAX, kinases such as hexokinases 1 and 2, cytoskeletal proteins such as tubulin and actin, etc. While Naghdi *et al.* (*8*) did not see an effect of N-terminal or cysteine deletion on BAK binding to VDAC2, these proteins could selectively recognize and bind a particular substate of VDAC2. Experimental validation of the BAX/BAK interaction at the single-molecule level remains challenging because of the pore-forming nature of these molecules. Nevertheless, the dynamic conformational flexibility identified in the present study may allow VDAC2 to recognize many such binding partners. Furthermore, our results demonstrate that αSyn-VDAC2 complexation could be a promising experimental approach to detect the subtle conformational changes of the single-membrane nanopore beyond that of VDACs. Together, VDAC2's role in apoptosis and redox sensing suggests that the NTE and cysteine residues alter VDAC2 channel properties for performing previously unknown nonredundant roles in eukaryotes, thus confirming the phylogenetic analysis of VDAC gene duplication in vertebrates (*90*).

The question as to why VDAC2 knockout is lethal or partially lethal, but knockouts of the other two isoforms are not, remains open. We speculate that VDAC2's unique plasticity, manifested by spontaneous transitions between high-conductance substates revealed in our in vitro single-channel experiments, could be a key to understanding its physiological significance. These data could tentatively explain the unique functional role of VDAC2 through its ability to dynamically adapt to rapidly changing metabolic cell conditions and to alter the rate of interaction with its presumably multiple protein partners. By elucidating how VDAC2's basic biophysical characteristics, such as its ability to stochastically switch between high-conductance substates, contribute to its physiological functions, we provide a deeper understanding of its unique role in cellular homeostasis.

Limitations to this study

This work focused on the biophysical study and mechanistic modeling of specifics and peculiarities of the VDAC2 channel. Therefore, translation of these observations to physiological implications in the native mitochondrial environment remains speculative. For these hypotheses about VDAC2 conformation to be tested in cells, the mutants described here can be reintroduced into VDAC2 knockout cell lines. We would expect mitochondrial functions to be altered and for the interactome (via an immunoprecipitation or proximity labeling strategy) to be shifted. Moreover, a more detailed understanding of the structural basis of VDAC2 substates would be enabled by a high-resolution crystal structure of hVDAC2.

MATERIALS AND METHODS

Cloning, recombinant protein production, and purification

Recombinant VDAC2 WT and VDAC2 E84A were purified and isolated as described in Supplementary Methods and stored in the buffer containing 25 mM Hepes (pH 7.4), 100 mM NaCl, 0.1% lauryldimethylamine oxide, 1 mM tris(2-carboxyethyl)phosphine, and 1 mM EDTA. The cysteine-less VDAC2 mutant (VDAC2-ΔCys) and VDAC2 mutant without NTE residues 1 to 11 (ΔN-VDAC2) were purified and isolated as previously described (*12*). Recombinant zebrafish VDAC2 (zfVDAC2) was a gift of J. Schredelseker (Walther Straub Institute of Pharmacology and Toxicology, Munich, Germany). Recombinant αSyn WT was a gift of J. Lee (National Heart, Lung, and Blood Institute, National Institutes of Health). αSyn was purified and characterized as described previously (*91*) and stored at −80°C.

VDAC reconstitution and conductance measurements

The procedure of VDAC reconstitution into lipid bilayers was described previously (*30*, *48*) and in Supplementary Methods. PLMs were formed from lipid mixtures of DOPG, dioleoylphosphatidylcholine, and dioleoyl-phosphatidylethanolamine in a ratio of 2:1:1 (w/w) in single-channel experiments or from soybean polar lipid extract in multichannel gating experiments. All lipids were purchased from Avanti Polar Lipids. Typically, channel insertion was achieved 2 to 20 min after the addition of 0.2 to 0.5 μl of VDAC2 diluted in 2.5% Triton X-100 buffer [50 mM KCl, 100 mM tris at pH 3.35, 1 mM EDTA, 15% (v/v) dimethyl sulfoxide, and 2.5% Triton X-100] on the Teflon partition facing the cis compartment. The potential is defined as positive when it is greater at the side of VDAC addition (cis side). Current recordings were performed as described previously (*30*) using an Axopatch 200B amplifier (Axon Instruments) in the voltage-clamp mode. Data were filtered by a low-pass eight-pole Butterworth filter (Model 900 Frequency Active Filter, Frequency Devices) at 15 kHz, digitized with a sampling frequency of 50 kHz, and analyzed using pClamp 10.7 software (Axon Instruments).

When a single VDAC channel was reconstituted into PLM and recorded, αSyn was added to both compartments of the experimental chamber to a 10 nM final concentration. For data analysis by Clampfit version 10.7, digital filtering using a 5-kHz low-pass Bessel (eight-pole) filter was applied. Individual events of current blockages were discriminated, and kinetic parameters were acquired by fitting logarithmic single exponentials to logarithmically binned histograms as described previously (*92*, *93*). All lifetime histograms used 10 bins per decade. The number of blockage events for each analyzed current fragment was in the range from 250 to 2500. Three different logarithmic probability fits were generated using different fitting algorithms, and the means and SD of the fitted time constants were used as the means and SD for the characteristic open and blockage times. Each channel experiment was repeated at least three times on different membranes. Records for analysis were obtained no less than 30 min after αSyn addition to ensure a steady state. Fits to histograms such as those in Fig. 3C used the maximum likelihood estimator with the simplex algorithm in Clampfit version 10.7.

VDAC ion selectivity was measured in a 1.0 M (cis) versus 0.2 M KCl (trans) gradient, buffered with 5 mM Hepes at pH 7.4, as described previously (*16*, *94*). The reversal potential—the potential corresponding to the zero-current level—was measured only for single channels either by application of a 5-mHz triangular voltage wave of ±50-mV amplitude or by measuring the current acquired at different applied voltages typically at 5-mV intervals. The Cl^-/K^+ permeability ratio was calculated using the Goldman-Hodgkin-Katz equation as previously described (*94*). VDAC voltage gating was measured on multichannel membranes using a previously described protocol (*43*, *48*, *95*) and in Supplementary Methods.

Thermal fluorescent protein stability assay

The melting temperatures (T_m) of recombinant VDAC were determined by native tryptophan fluorescence using a Tycho Differential Scanning Fluorometer (Nanotemper). VDAC samples were diluted to 1 mg/ml in 25 mM Hepes at pH 7.4, 100 mM NaCl, 0.1% lauryldimethylamine oxide, 1 mM tris(2-carboxyethyl)phosphine, and 1 mM EDTA buffer. The ratio of 350- to 330-nm native tryptophan fluorescence increases at higher temperatures because of exposure of unfolded tryptophan to the solution. The T_m was determined from the inflection point of the curve.

Statistical analysis

ECDFs were calculated on the basis of observed conductances using the Python package iqplot. To determine the confidence interval for the ECDF, 1000 bootstrap replicates were used. The shaded region on the ECDF plots represents the 95% confidence interval derived from the bootstrap analysis. To evaluate the change in substate occurrences for a given mutant or the probability that a channel will display substates for a given number of observations, we modeled the process as being generated by the binomial equation and calculated the maximum likelihood estimation (MLE) for the binomial coefficient. The MLE for the binomial coefficient to estimate the proportion of channels with substates for each mutant was computed on the basis of 25, 27, and 16 observations for the VDAC2 WT, ΔN-VDAC2, and VDAC2-ΔCys channels, respectively. A total of 10,000 bootstrapped replicates was generated. Significance was determined using a chi-square test.

Supplementary Materials

This PDF file includes:

Supplementary Methods
Figs. S1 to S6

REFERENCES AND NOTES

1. Z. Rahmani, C. Maunoury, A. Siddiqui, Isolation of a novel human voltage-dependent anion channel gene. *Eur. J. Hum. Genet.* **6**, 337–340 (1998).
2. A. Messina, S. Reina, F. Guarino, V. De Pinto, VDAC isoforms in mammals. *Biochim. Biophys. Acta* **1818**, 1466–1476 (2012).
3. P. D. Piehowski, Y. Zhu, L. M. Bramer, K. G. Stratton, R. Zhao, D. J. Orton, R. J. Moore, J. Yuan, H. D. Mitchell, Y. Gao, B. M. Webb-Robertson, S. K. Dey, R. T. Kelly, K. E. Burnum-Johnson, Automated mass spectrometry imaging of over 2000 proteins from tissue sections at 100-μm spatial resolution. *Nat. Commun.* **11**, 8 (2020).
4. K. Anflous-Pharayra, N. Lee, D. L. Armstrong, W. J. Craigen, VDAC3 has differing mitochondrial functions in two types of striated muscles. *Biochim. Biophys. Acta* **1807**, 150–156 (2011).
5. M. J. Sampson, W. K. Decker, A. L. Beaudet, W. Ruitenbeek, D. Armstrong, M. J. Hicks, W. J. Craigen, Immotile sperm and infertility in mice lacking mitochondrial voltage-dependent anion channel type 3. *J. Biol. Chem.* **276**, 39206–39212 (2001).
6. E. H. Y. Cheng, T. V. Sheiko, J. K. Fisher, W. J. Craigen, S. J. Korsmeyer, VDAC2 inhibits BAK activation and mitochondrial apoptosis. *Science* **301**, 513–517 (2003).
7. H. S. Chin, M. X. Li, I. K. L. Tan, R. L. Ninnis, B. Reljic, K. Scicluna, L. F. Dagley, J. J. Sandow, G. L. Kelly, A. L. Samson, S. Chappaz, S. L. Khaw, C. Chang, A. Morokoff, K. Brinkmann, A. Webb, C. Hockings, C. M. Hall, A. J. Kueh, M. T. Ryan, R. M. Kluck, P. Bouillet, M. J. Herold, D. H. D. Gray, D. C. S. Huang, M. F. van Delft, G. Dewson, VDAC2 enables BAX to mediate apoptosis and limit tumor development. *Nat. Commun.* **9**, 4976 (2018).
8. S. Naghdi, P. Varnai, G. Hajnoczky, Motifs of VDAC2 required for mitochondrial Bak import and tBid-induced apoptosis. *Proc. Natl. Acad. Sci. U.S.A.* **112**, E5590–E5599 (2015).

9. M. Lazarou, D. Stojanovski, A. E. Frazier, A. Kotevski, G. Dewson, W. J. Craigen, R. M. Kluck, D. L. Vaux, M. T. Ryan, Inhibition of Bak activation by VDAC2 is dependent on the Bak transmembrane anchor. *J. Biol. Chem.* **285**, 36876–36883 (2010).
10. S. Callegari, N. S. Kirk, Z. Y. Gan, T. Dite, S. A. Cobbold, A. Leis, L. F. Dagley, A. Glukhova, D. Komander, Structure of human PINK1 at a mitochondrial TOM-VDAC array. *Science* , eadu6445 (2025).
11. V. De Pinto, Renaissance of VDAC: New insights on a protein family at the interface between mitochondria and cytosol. *Biomolecules* **11**, 107 (2021).
12. S. R. Maurya, R. Mahalakshmi, N-helix and cysteines inter-regulate human mitochondrial VDAC-2 function and biochemistry. *J. Biol. Chem.* **290**, 30240–30252 (2015).
13. X. Xu, W. Decker, M. J. Sampson, W. J. Craigen, M. Colombini, Mouse VDAC isoforms expressed in yeast: Channel properties and their roles in mitochondrial outer membrane permeability. *J. Membr. Biol.* **170**, 89–102 (1999).
14. S. R. Maurya, R. Mahalakshmi, Modulation of human mitochondrial voltage-dependent anion channel 2 (hVDAC-2) structural stability by cysteine-assisted barrel-lipid interactions. *J. Biol. Chem.* **288**, 25584–25592 (2013).
15. V. A. Menzel, M. C. Cassará, R. Benz, V. de Pinto, A. Messina, V. Cunsolo, R. Saletti, K.-D. Hinsch, E. Hinsch, Molecular and functional characterization of VDAC2 purified from mammal spermatozoa. *Biosci. Rep.* **29**, 351–362 (2009).
16. W. M. Rosencrans, V. M. Aguilella, T. K. Rostovtseva, S. M. Bezrukov, α-Synuclein emerges as a potent regulator of VDAC-facilitated calcium transport. *Cell Calcium* **95**, 102355 (2021).
17. M. Goedert, R. Jakes, M. G. Spillantini, The synucleinopathies: Twenty years on. *J. Parkinsons Dis.* **7**, S51–S69 (2017).
18. W. S. Kim, K. Kågedal, G. M. Halliday, Alpha-synuclein biology in Lewy body diseases. *Alzheimers Res. Ther.* **6**, 73 (2014).
19. M. G. Spillantini, M. L. Schmidt, V. M.-Y. Lee, J. Q. Trojanowski, R. Jakes, M. Goedert, α-Synuclein in Lewy bodies. *Nature* **388**, 839–840 (1997).
20. J. Parres-Gold, A. Chieng, S. Wong Su, Y. Wang, Real-time characterization of cell membrane disruption by α-synuclein oligomers in live SH-SY5Y neuroblastoma cells. *ACS Chem. Nerosci.* **11**, 2528–2534 (2020).
21. H. Elkon, J. Don, E. Melamed, I. Ziv, A. Shirvan, D. Offen, Mutant and wild-type α-synuclein interact with mitochondrial cytochrome C oxidase. *J. Mol. Neurosci.* **18**, 229–238 (2002).
22. L. Devi, V. Raghavendran, B. M. Prabhu, N. G. Avadhani, H. K. Anandatheerthavarada, Mitochondrial import and accumulation of α-synuclein impair complex I in human dopaminergic neuronal cultures and Parkinson disease brain. *J. Biol. Chem.* **283**, 9089–9100 (2008).
23. M. H. R. Ludtmann, P. R. Angelova, M. H. Horrocks, M. L. Choi, M. Rodrigues, A. Y. Baev, A. V. Berezhnov, Z. Yao, D. Little, B. Banushi, A. S. Al-Menhali, R. T. Ranasinghe, D. R. Whiten, R. Yapom, K. S. Dolt, M. J. Devine, P. Gissen, T. Kunath, M. Jaganjac, E. V. Pavlov, D. Klenerman, A. Y. Abramov, S. Gandhi, α-synuclein oligomers interact with ATP synthase and open the permeability transition pore in Parkinson's disease. *Nat. Commun.* **9**, 2293 (2018).
24. L. J. Hsu, Y. Sagara, A. Arroyo, E. Rockenstein, A. Sisk, M. Mallory, J. Wong, T. Takenouchi, M. Hashimoto, E. Masliah, α-Synuclein promotes mitochondrial deficit and oxidative stress. *Am. J. Pathol.* **157**, 401–410 (2000).
25. S. J. Chinta, J. K. Mallajosyula, A. Rane, J. K. Andersen, Mitochondrial alpha-synuclein accumulation impairs complex I function in dopaminergic neurons and results in increased mitophagy in vivo. *Neurosci. Lett.* **486**, 235–239 (2010).
26. K. Nakamura, V. M. Nemani, F. Azarbal, G. Skibinski, J. M. Levy, K. Egami, L. Munishkina, J. Zhang, B. Gardner, J. Wakabayashi, H. Sesaki, Y. Cheng, S. Finkbeiner, R. L. Nussbaum, E. Masliah, R. H. Edwards, Direct membrane association drives mitochondrial fission by the Parkinson disease-associated protein α-synuclein. *J. Biol. Chem.* **286**, 20710–20726 (2011).
27. A. Magri, A. Messina, Interactions of VDAC with proteins involved in neurodegenerative aggregation: An opportunity for advancement on therapeutic molecules. *Curr. Med. Chem.* **24**, 4470–4487 (2017).
28. A. Rovini, P. A. Gurnev, A. Beilina, M. Queralt-Martín, W. Rosencrans, M. R. Cookson, S. M. Bezrukov, T. K. Rostovtseva, Molecular mechanism of olesoxime-mediated neuroprotection through targeting α-synuclein interaction with mitochondrial VDAC. *Cell. Mol. Life Sci.* **77**, 3611–3626 (2020).
29. M. Rajendran, M. Queralt-Martin, P. A. Gurnev, W. M. Rosencrans, A. Rovini, D. Jacobs, K. Abrantes, D. P. Hoogerheide, S. M. Bezrukov, T. K. Rostovtseva, Restricting α-synuclein transport into mitochondria by inhibition of α-synuclein-VDAC complexation as a potential therapeutic target for Parkinson's disease treatment. *Cell. Mol. Life Sci.* **79**, 368 (2022).
30. T. K. Rostovtseva, P. A. Gurnev, O. Protchenko, D. P. Hoogerheide, T. L. Yap, C. C. Philpott, J. C. Lee, S. M. Bezrukov, α-Synuclein shows high affinity interaction with voltage-dependent anion channel, suggesting mechanisms of mitochondrial regulation and toxicity in Parkinson disease. *J. Biol. Chem.* **290**, 18467–18477 (2015).
31. T. S. Ulmer, A. Bax, Comparison of structure and dynamics of micelle-bound human α-synuclein and Parkinson disease variants. *J. Biol. Chem.* **280**, 43179–43187 (2005).
32. D. Eliezer, E. Kutluay, R. Bussell Jr., G. Browne, Conformational properties of α-synuclein in its free and lipid-associated states. *J. Mol. Biol.* **307**, 1061–1073 (2001).
33. G. Fusco, A. De Simone, T. Gopinath, V. Vostrikov, M. Vendruscolo, C. M. Dobson, G. Veglia, Direct observation of the three regions in α-synuclein that determine its membrane-bound behaviour. *Nat. Commun.* **5**, 3827 (2014).
34. D. P. Hoogerheide, T. K. Rostovtseva, S. M. Bezrukov, Exploring lipid-dependent conformations of membrane-bound α-synuclein with the VDAC nanopore. *Biochim. Biophys. Acta Biomembr.* **1863**, 183643 (2021).
35. D. P. Hoogerheide, P. A. Gurnev, T. K. Rostovtseva, S. M. Bezrukov, Real-time nanopore-based recognition of protein translocation success. *Biophys. J.* **114**, 772–776 (2018).
36. P. A. Gurnev, T. K. Rostovtseva, S. M. Bezrukov, Tubulin-blocked state of VDAC studied by polymer and ATP partitioning. *FEBS Lett.* **585**, 2363–2366 (2011).
37. P. A. Gurnev, T. L. Yap, C. M. Pfefferkorn, T. K. Rostovtseva, A. M. Berezhkovskii, J. C. Lee, V. A. Parsegian, S. M. Bezrukov, Alpha-synuclein lipid-dependent membrane binding and translocation through the α-hemolysin channel. *Biophys. J.* **106**, 556–565 (2014).
38. T. Cali, D. Ottolini, A. Negro, M. Brini, α-Synuclein controls mitochondrial calcium homeostasis by enhancing endoplasmic reticulum-mitochondria interactions. *J. Biol. Chem.* **287**, 17914–17929 (2012).
39. M. Queralt-Martin, L. Bergdoll, O. Teijido, N. Munshi, D. Jacobs, A. J. Kuszak, O. Protchenko, S. Reina, A. Magri, V. De Pinto, S. M. Bezrukov, J. Abramson, T. K. Rostovtseva, A lower affinity to cytosolic proteins reveals VDAC3 isoform-specific role in mitochondrial biology. *J. Gen. Physiol.* **152**, e201912501 (2020).
40. W. M. Rosencrans, M. Rajendran, S. M. Bezrukov, T. K. Rostovtseva, VDAC regulation of mitochondrial calcium flux: From channel biophysics to disease. *Cell Calcium* **94**, 102356 (2021).
41. M. T. Eddy, T. C. Ong, L. Clark, O. Teijido, P. C. van der Wel, R. Garces, G. Wagner, T. K. Rostovtseva, R. G. Griffin, Lipid dynamics and protein–lipid interactions in 2D crystals formed with the β-barrel integral membrane protein VDAC1. *J. Am. Chem. Soc.* **134**, 6375–6387 (2012).
42. M. Queralt-Martín, L. Bergdoll, D. Jacobs, S. M. Bezrukov, J. Abramson, T. K. Rostovtseva, Assessing the role of residue E73 and lipid headgroup charge in VDAC1 voltage gating. *Biochim. Biophys. Acta Bioenerg.* **1860**, 22–29 (2019).
43. M. Colombini, Voltage gating in the mitochondrial channel, VDAC. *J. Membr. Biol.* **111**, 103–111 (1989).
44. D. P. Hoogerheide, P. A. Gurnev, T. K. Rostovtseva, S. M. Bezrukov, Voltage-activated complexation of α-synuclein with three diverse β-barrel channels: VDAC, MspA, and α-hemolysin. *Proteomics* **22**, 2100060 (2022).
45. D. Jacobs, D. P. Hoogerheide, A. Rovini, Z. Jiang, J. C. Lee, T. K. Rostovtseva, S. M. Bezrukov, Probing membrane association of α-synuclein domains with VDAC nanopore reveals unexpected binding pattern. *Sci. Rep.* **9**, 4580 (2019).
46. T. S. Ulmer, A. Bax, N. B. Cole, R. L. Nussbaum, Structure and dynamics of micelle-bound human α-synuclein. *J. Biol. Chem.* **280**, 9595–9603 (2005).
47. C. M. Pfefferkorn, Z. Jiang, J. C. Lee, Biophysics of α-synuclein membrane interactions. *Biochim. Biophys. Acta* **1818**, 162–171 (2012).
48. T. K. Rostovtseva, N. Kazemi, M. Weinrich, S. M. Bezrukov, Voltage gating of VDAC is regulated by nonlamellar lipids of mitochondrial membranes. *J. Biol. Chem.* **281**, 37496–37506 (2006).
49. S. R. Maurya, R. Mahalakshmi, Mitochondrial VDAC2 and cell homeostasis: Highlighting hidden structural features and unique functionalities. *Biol. Rev. Camb. Philos. Soc.* **92**, 1843–1858 (2017).
50. V. De Pinto, S. Reina, A. Gupta, A. Messina, R. Mahalakshmi, Role of cysteines in mammalian VDAC isoforms' function. *Biochim. Biophys. Acta* **1857**, 1219–1227 (2016).
51. S. R. Maurya, R. Mahalakshmi, Influence of protein-micelle ratios and cysteine residues on the kinetic stability and unfolding rates of human mitochondrial VDAC-2. *PLOS ONE* **9**, e87701 (2014).
52. D. P. Hoogerheide, P. A. Gurnev, T. K. Rostovtseva, S. M. Bezrukov, Effect of a post-translational modification mimic on protein translocation through a nanopore. *Nanoscale* **12**, 11070–11078 (2020).
53. A. B. Rister, T. Gudermann, J. Schredelseker, E as in enigma: The mysterious role of the voltage-dependent anion channel glutamate E73. *Int. J. Mol. Sci.* **24**, 269 (2023).
54. A. Israelson, S. Abu-Hamad, H. Zaid, E. Nahon, V. Shoshan-Barmatz, Localization of the voltage-dependent anion channel-1 Ca^{2+}-binding sites. *Cell Calcium* **41**, 235–244 (2007).
55. S. Hiller, J. Abramson, C. Mannella, G. Wagner, K. Zeth, The 3D structures of VDAC represent a native conformation. *Trends Biochem. Sci.* **35**, 514–521 (2010).
56. M. Colombini, The published 3D structure of the VDAC channel: Native or not? *Trends Biochem. Sci.* **34**, 382–389 (2009).
57. M. Bayrhuber, T. Meins, M. Habeck, S. Becker, K. Giller, S. Villinger, C. Vonrhein, C. Griesinger, M. Zweckstetter, K. Zeth, Structure of the human voltage-dependent anion channel. *Proc. Natl. Acad. Sci. U.S.A.* **105**, 15370–15375 (2008).
58. S. Villinger, R. Briones, K. Giller, U. Zachariae, A. Lange, B. L. de Groot, C. Griesinger, S. Becker, M. Zweckstetter, Functional dynamics in the voltage-dependent anion channel. *Proc. Natl. Acad. Sci. U.S.A.* **107**, 22546–22551 (2010).

59. V. A. Ngo, M. Queralt-Martin, F. Khan, L. Bergdoll, J. Abramson, S. M. Bezrukov, T. K. Rostovtseva, D. P. Hoogerheide, S. Y. Noskov, The single residue K12 governs the exceptional voltage sensitivity of mitochondrial voltage-dependent anion channel gating. *J. Am. Chem. Soc.* **144**, 14564–14577 (2022).
60. S. Dadsena, S. Bockelmann, J. G. M. Mina, D. G. Hassan, S. Korneev, G. Razzera, H. Jahn, P. Niekamp, D. Muller, M. Schneider, F. G. Tafesse, S. J. Marrink, M. N. Melo, J. C. M. Holthuis, Ceramides bind VDAC2 to trigger mitochondrial apoptosis. *Nat. Commun.* **10**, 1832 (2019).
61. L. Mlayeh, E.-M. Krammer, M. Leonetti, M. Prévost, F. Homblé, The mitochondrial VDAC of bean seeds recruits phosphatidylethanolamine lipids for its proper functioning. *Biochim. Biophys. Acta Bioenerg.* **1858**, 786–794 (2017).
62. L. Mlayeh, S. Chatkaew, M. Léonetti, F. Homblé, Modulation of plant mitochondrial VDAC by phytosterols. *Biophys. J.* **99**, 2097–2106 (2010).
63. C. Guardiani, A. Magri, A. Karachitos, M. C. Di Rosa, S. Reina, I. Bodrenko, A. Messina, H. Kmita, M. Ceccarelli, V. De Pinto, yVDAC2, the second mitochondrial porin isoform of *Saccharomyces cerevisiae*. *Biochim. Biophys. Acta Bioenerg.* **1859**, 270–279 (2018).
64. Z. Gattin, R. Schneider, Y. Laukat, K. Giller, E. Maier, M. Zweckstetter, C. Griesinger, R. Benz, S. Becker, A. Lange, Solid-state NMR, electrophysiology and molecular dynamics characterization of human VDAC2. *J. Biomol. NMR* **61**, 311–320 (2015).
65. M. T. Eddy, T. Y. Yu, G. Wagner, R. G. Griffin, Structural characterization of the human membrane protein VDAC2 in lipid bilayers by MAS NMR. *J. Biomol. NMR* **73**, 451–460 (2019).
66. R. Ujwal, D. Cascio, V. Chaptal, P. Ping, J. Abramson, Crystal packing analysis of murine VDAC1 crystals in a lipidic environment reveals novel insights on oligomerization and orientation. *Channels* **3**, 167–170 (2009).
67. U. Zachariae, R. Schneider, R. Briones, Z. Gattin, J. P. Demers, K. Giller, E. Maier, M. Zweckstetter, C. Griesinger, S. Becker, R. Benz, B. L. de Groot, A. Lange, β-barrel mobility underlies closure of the voltage-dependent anion channel. *Structure* **20**, 1540–1549 (2012).
68. J. Schredelseker, A. Paz, C. J. López, C. Altenbach, C. S. Leung, M. K. Drexler, J.-N. Chen, W. L. Hubbell, J. Abramson, High resolution structure and double electron-electron resonance of the zebrafish voltage-dependent anion channel 2 reveal an oligomeric population. *J. Biol. Chem.* **289**, 12566–12577 (2014).
69. J. Song, C. Midson, E. Blachly-Dyson, M. Forte, M. Colombini, The topology of VDAC as probed by biotin modification. *J. Biol. Chem.* **273**, 24406–24413 (1998).
70. L. Thomas, E. Blachly-Dyson, M. Colombini, M. Forte, Mapping of residues forming the voltage sensor of the voltage-dependent anion-selective channel. *Proc. Natl. Acad. Sci. U.S.A.* **90**, 5446–5449 (1993).
71. J. Song, C. Midson, E. Blachly-Dyson, M. Forte, M. Colombini, The sensor regions of VDAC are translocated from within the membrane to the surface during the gating processes. *Biophys. J.* **74**, 2926–2944 (1998).
72. M. A. Aksoyoglu, R. Podgornik, S. M. Bezrukov, P. A. Gurnev, M. Muthukumar, V. A. Parsegian, Size-dependent forced PEG partitioning into channels: VDAC, OmpC, and α-hemolysin. *Proc. Natl. Acad. Sci. U.S.A.* **113**, 9003–9008 (2016).
73. I. Vodyanoy, S. M. Bezrukov, Sizing of an ion pore by access resistance measurements. *Biophys. J.* **62**, 10–11 (1992).
74. M. Aguilella-Arzo, V. M. Aguilella, Access resistance in protein nanopores. A structure-based computational approach. *Bioelectrochemistry* **131**, 107371 (2020).
75. M. Gershow, J. A. Golovchenko, Recapturing and trapping single molecules with a solid-state nanopore. *Nat. Nanotechnol.* **2**, 775–779 (2007).
76. M. Wanunu, W. Morrison, Y. Rabin, A. Y. Grosberg, A. Meller, Electrostatic focusing of unlabelled DNA into nanoscale pores using a salt gradient. *Nat. Nanotechnol.* **5**, 160–165 (2010).
77. B. Hille, *Ion Channels of Excitable Membranes* (Sinauer Associates Inc., ed. 3, 2001), vol. 3.
78. M. Muthukumar, Theory of capture rate in polymer translocation. *J. Chem. Phys.* **132**, 195101 (2010).
79. S. R. Maurya, R. Mahalakshmi, VDAC-2: Mitochondrial outer membrane regulator masquerading as a channel? *FEBS J.* **283**, 1831–1836 (2016).
80. W. A. T. Summers, J. A. Wilkins, R. C. Dwivedi, P. Ezzati, D. A. Court, Mitochondrial dysfunction resulting from the absence of mitochondrial porin in *Neurospora crassa*. *Mitochondrion* **12**, 220–229 (2012).
81. K. A. Diederichs, S. K. Buchanan, I. Botos, Building better barrels – β-barrel biogenesis and insertion in bacteria and mitochondria. *J. Mol. Biol.* **433**, 166894 (2021).
82. D. C. Bay, M. Hafez, M. J. Young, D. A. Court, Phylogenetic and coevolutionary analysis of the β-barrel protein family comprised of mitochondrial porin (VDAC) and Tom40. *Biochim. Biophys. Acta* **1818**, 1502–1519 (2012).
83. Y. Araiso, T. Endo, Structural overview of the translocase of the mitochondrial outer membrane complex. *Biophys. Physicobiol.* **19**, e190022 (2022).
84. W. Tan, M. Colombini, VDAC closure increases calcium ion flux. *Biochim. Biophys. Acta* **1768**, 2510–2515 (2007).
85. T. Rostovtseva, M. Colombini, ATP flux is controlled by a voltage-gated channel from the mitochondrial outer membrane. *J. Biol. Chem.* **271**, 28006–28008 (1996).
86. T. K. Rostovtseva, A. Komarov, S. M. Bezrukov, M. Colombini, Dynamics of nucleotides in VDAC channels: Structure-specific noise generation. *Biophys. J.* **82**, 193–205 (2002).
87. A. Karachitos, W. Grabinski, M. Baranek, H. Kmita, Redox-sensitive VDAC: A possible function as an environmental stress sensor revealed by bioinformatic analysis. *Front. Physiol.* **12**, 750627 (2021).
88. M. G. G. Pittala, S. Reina, A. Cucina, V. Cunsolo, F. Guarino, A. Di Francesco, S. Foti, V. De Pinto, R. Saletti, Intramolecular disulfide bridges in Voltage-Dependent Anion Channel 2 (VDAC2) protein from *Rattus norvegicus* revealed by high-resolution mass spectrometry. *J. Am. Soc. Mass Spectrom.* **35**, 1422–1433 (2024).
89. S. Reina, S. C. Nibali, M. F. Tomasello, A. Magri, A. Messina, V. De Pinto, Voltage Dependent Anion Channel 3 (VDAC3) protects mitochondria from oxidative stress. *Redox Biol.* **51**, 102264 (2022).
90. C. Saccone, C. Caggese, A. M. D'Erchia, C. Lanave, M. Oliva, G. Pesole, Molecular clock and gene function. *J. Mol. Evol.* **57**, S277–S285 (2003).
91. C. M. Pfefferkorn, J. C. Lee, Tryptophan probes at the α-synuclein and membrane interface. *J. Phys. Chem. B* **114**, 4615–4622 (2010).
92. F. J. Sigworth, S. M. Sine, Data transformations for improved display and fitting of single-channel dwell time histograms. *Biophys. J.* **52**, 1047–1054 (1987).
93. M. Weinrich, D. L. Worcester, S. M. Bezrukov, Lipid nanodomains change ion channel function. *Nanoscale* **9**, 13291–13297 (2017).
94. O. Teijido, S. M. Rappaport, A. Chamberlin, S. Y. Noskov, V. M. Aguilella, T. K. Rostovtseva, S. M. Bezrukov, Acidification asymmetrically affects voltage-dependent anion channel implicating the involvement of salt bridges. *J. Biol. Chem.* **289**, 23670–23682 (2014).
95. S. M. Rappaport, O. Teijido, D. P. Hoogerheide, T. K. Rostovtseva, A. M. Berezhkovskii, S. M. Bezrukov, Conductance hysteresis in the voltage-dependent anion channel. *Eur. Biophys. J.* **44**, 465–472 (2015).

Acknowledgments: We thank D. Hoogerheide and M. Rajendran for discussions and for reading our manuscript. W.M.R, M.G.L, T.K.R., and S.M.B. were supported by the Intramural Research Program of the Eunice Kennedy Shriver National Institute of Child Health and Human Development of the National Institutes of Health. This research was funded in part by a gift from the J. Yang and Family Foundation. **Funding:** This work was supported by the following: National Institutes of Health grant ZIA HD000072-18 (to S.M.B.) and Wellcome Trust–Department of Biotechnology India Alliance grant IA/S/20/2/505182 (to R.M.). **Author contributions:** Conceptualization: T.K.R., S.M.B., W.M.R., and M.G.L. Methodology: T.K.R., S.M.B., W.M.R., and T.-Y.Y. Software: W.M.R. Validation: W.M.R., T.K.R., S.M.B., H.K., M.G.L., and T.-Y.Y. Formal analysis: W.M.R., T.K.R., S.M.B., and T.-Y.Y. Investigation: W.M.R., T.K.R., M.G.L., and T.-Y.Y. Resources: T.K.R., S.M.B., W.M.R., R.M., H.K., and T.-Y.Y. Data curation: W.M.R., T.K.R., S.M.B., and T.-Y.Y. Writing—original draft: T.K.R., W.M.R., S.M.B., and T.-Y.Y. Writing—review and editing: T.K.R., W.M.R., S.M.B., M.G.L., and T.-Y.Y. Visualization: W.M.R., T.K.R., S.M.B., M.G.L., and T.-Y.Y. Supervision: T.K.R. and S.M.B. Project administration: T.K.R., S.M.B., and W.M.R. Funding acquisition: S.M.B., W.M.R., and R.M. **Competing interests:** The authors declare that they have no competing interests. **Data and materials availability:** All data needed to evaluate the conclusions in the paper are present in the paper and/or the Supplementary Materials.

Submitted 19 December 2024
Accepted 17 March 2025
Published 23 April 2025
10.1126/sciadv.adv4410